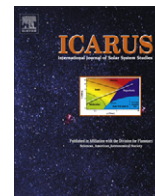




Contents lists available at ScienceDirect

Icarus

journal homepage: [www.elsevier.com/locate/icarus](http://www.elsevier.com/locate/icarus)

## Vertical structure of Jupiter's Oval BA before and after it reddened: What changed? <sup>☆</sup>

Michael H. Wong <sup>a,\*</sup>, Imke de Pater <sup>a</sup>, Xylar Asay-Davis <sup>b</sup>, Philip S. Marcus <sup>c</sup>, Christopher Y. Go <sup>d</sup>

<sup>a</sup> Astronomy Department, University of California, Berkeley, CA 94720-3411, USA

<sup>b</sup> Los Alamos National Laboratory, Los Alamos, NM 87545, USA

<sup>c</sup> Department of Mechanical Engineering, University of California, Berkeley, CA 94720-1740, USA

<sup>d</sup> Physics Department, University of San Carlos, 6000 Cebu City, Philippines

### ARTICLE INFO

#### Article history:

Received 4 September 2010

Revised 17 June 2011

Accepted 21 June 2011

Available online xxxxx

#### Keywords:

Jupiter, Atmosphere

Atmospheres, Structure

Atmospheres, Dynamics

Abundances, Atmospheres

Hubble Space Telescope observations

### ABSTRACT

To constrain the properties of Oval BA before and after it reddened, we use Hubble methane band images from 1994 to 2009 to find that the distribution of upper tropospheric haze atop the oval and its progenitors remained unchanged, with reflectivity variations of less than 10% over this time span. We quantify measurement uncertainties and short-term fluctuations in velocity fields extracted from Cassini and Hubble data, and show that there were no significant changes in the horizontal velocity field of Oval BA in 2000, 2006, and 2009. Based on models of the oval's dynamics, the static stability of the oval's surroundings was also unchanged.

The vertical extent of the oval did not change, based on the unchanged haze reflectivity and unchanged stratification. Published vortex models require Brunt–Väisälä frequencies of about  $0.08 \text{ s}^{-1}$  at the base of the vortex, and we combine this value with a review of prior constraints on the vertically variable static stability in Jupiter's troposphere to show that the vortex must extend down to the condensation level of water in supersolar abundance.

The only observable change was an increase in short-wavelength optical absorption that appeared not at the core of the oval, but in a red annulus. The secondary circulation in the vortex keeps this red annulus warmer than the vortex core. Although the underlying cause of the color change cannot be proven, we explore the idea that the new chromophores in the red annulus may be related to a global or hemispheric temperature change.

© 2011 Elsevier Inc. All rights reserved.

### 1. Introduction

Oval BA turned red in December 2005 (Go et al., 2006), joining the Great Red Spot (GRS) in the small family of persistent red anticyclonic vortices on Jupiter, although smaller transient red vortices have been previously identified (Beebe and Hockey, 1986; de Pater et al., 2010b). No red coloring agent (or chromophore) has been conclusively identified for Oval BA or the GRS, but several candidates have been proposed. Oval BA formed between 1998 and 2000 from the precursor White Ovals DE, FA, and BC (Sánchez-Lavega et al., 1999, 2001), after they became trapped in the trough of a Rossby wave with no intervening cyclones (Youssef and Marcus, 2003). The color change took place about 6 years after the merger, slightly longer than the radiative timescale in the upper troposphere (Gierasch and Goody, 1969; Flasar, 1989; Conrath et al.,

1990). Before they merged, these three White Ovals had coexisted near  $33^\circ\text{S}$  since their formation in 1939–1940 (Peek, 1958).

In this paper, we investigate several properties of Oval BA before and after its color change: its velocity field (Section 3), the reflectivity of its upper tropospheric haze (Section 4), and its thermodynamic structure (Section 5). Published numerical models of Oval BA and similar vortices constrain the static stability of the atmosphere in the surroundings of the vortex, but these models did not simulate vertical variation in the static stability of Jupiter's atmosphere. The variability of static stability can act as a measuring stick to determine the pressure level of Oval BA's base, which cannot be observed directly because it is beneath the clouds. The published vortex models correspond to static stability that is characteristic of the water cloud layer, with water in supersolar abundance. Within the uncertainties of the velocity fields and vortex models, the base of Oval BA, and the rest of its vertical structure, did not change before and after the color change. In fact, we find no significant changes other than the oval's color. In discussing potential chromophore processes involved in the oval's reddening, we find further support for the possibility that the color change is consistent with a modest temperature increase in Jupiter's southern hemisphere (de Pater et al., 2010b; Marcus et al., 2011).

<sup>☆</sup> Based on observations made with the NASA/ESA Hubble Space Telescope, obtained at the Space Telescope Science Institute, which is operated by the Association of Universities for Research in Astronomy, Inc., under NASA contract NAS 5-26555.

\* Corresponding author. Fax: +1 510 642 3411.

E-mail address: [mikewong@astro.berkeley.edu](mailto:mikewong@astro.berkeley.edu) (M.H. Wong).

**Table 1**  
Identification of data used to measure velocity fields, chromophore distribution, and haze reflectivity.

Facility	Date	Identifier	Separation interval	Frames	Applications
Hubble/WFC3	2009-09-18	Program 11559	10 h 22 m	30 <sup>*</sup>	Velocity, color, haze reflectivity
Hubble/ACS	2006-04-24	Program 10782	9 h 59 m	8 <sup>*</sup>	Color, velocity, haze reflectivity
Hubble/ACS	2005-01-19	Program 10192	–	4	Haze reflectivity
Cassini/ISS	2000-12-12	ISS_C23RI_RM0V020	11 h 34 m	12 <sup>*</sup>	Velocity
Hubble/WFPC2	2008-05-10	Program 11102	–	2	Haze reflectivity
Hubble/WFPC2	2008-05-09	Program 11102	–	3	Haze reflectivity
Hubble/WFPC2	2007-03-08	Program 10782	–	4	Haze reflectivity
Hubble/WFPC2	2000-09-02	Program 8871	–	6	Haze reflectivity
Hubble/WFPC2	1998-07-16	Program 7616	–	13	Haze reflectivity
Hubble/WFPC2	1997-06-25	Program 6452	–	6	Haze reflectivity
Hubble/WFPC2	1997-04-04	Program 6452	–	12	Haze reflectivity
Hubble/WFPC2	1995-02-17	Program 5313	–	12	Haze reflectivity
Hubble/WFPC2	1995-02-13	Program 5313	–	8	Haze reflectivity

<sup>\*</sup> Number of image *pairs* used for velocity field retrieval.

## 2. Observations

High resolution Hubble Space Telescope (HST) images in the methane gas absorption band from before and after the color change are used to measure potential variability in the oval's tropospheric haze reflectivity, as well as in the spatial distribution of red (blue-absorbing) aerosols. These data, along with Cassini Imaging (ISS) data, were also used to derive horizontal velocity fields. Here we discuss observational details, with the analysis of the imaging data to follow in Sections 3 and 4.

### 2.1. Methane-band and color imaging

Images of Jupiter at wavelengths near 890 nm are primarily sensitive to variations in the opacity of the upper tropospheric haze. The haze opacity above large jovian anticyclones has greater optical depth and vertical extent than in the surrounding upper troposphere. Radiative transfer modeling establishes that the top of the haze over Oval BA (or its progenitors) reaches to just below the tropopause, with reported upper boundaries of 150 mbar (Banfield et al., 1998b), 100–250 mbar (Pérez-Hoyos et al., 2009), or 200 mbar (de Pater et al., 2010b). The measured reflectivity depends on the haze density, haze vertical distribution, and optical path length (as determined by the emission and incidence angles).

HST Wide Field Planetary Camera 2 (WFPC2) data span the longest timeframe, covering 1994–2000 and 2007–2008 (see Table 1). Methane-band imaging data from HST's Advanced Camera for Surveys (ACS) and High Resolution Channel (HRC) were also used from both 2005 and 2006, before and after the color change. Data from the HRC in 2006 were the first high-resolution images to show the red coloration of Oval BA (Fig. 1). The WFPC2 and ACS instruments are described respectively in McMaster and Biretta (2008) and Maybhate (2010). The imaging data were converted to  $I/F$  using Eq. (1) of Sromovsky and Fry (2002). Cosmic ray strikes and geometric distortion were removed using crutil and drizzle within PyRAF, and L.A.COSMIC.<sup>1</sup>

Finally, the processed images were deprojected into latitude–longitude space by fitting the limb of Jupiter where available, or by matching multiple cloud features to other limb-fitted images where no limb was available within the image. The full analysis procedure, with emphasis on the deprojection using custom soft-



**Fig. 1.** Cylindrical projection from HST images of the Great Red Spot and Oval BA. Map spans longitudes of 225°–298°W (System III) and planetographic latitudes of 0° to –48°. Each channel has been stretched to span the maximum range of contrast for display. Red coloration in Oval BA is absent from the core of the vortex. (For interpretation of the references to color in this figure legend, the reader is referred to the web version of this article.)

ware, has been described in more detail in Asay-Davis et al. (2009) and Lii et al. (2010).

In 2009, we observed Jupiter with the newly-installed Wide Field Camera 3, or WFC3 (Wong et al., 2010), and used the same data reduction processes described above. Calibration uncertainties for WFC3 data in the methane-band filter will be reduced over time, but at this point are greater for WFC3 data than for other HST instruments. Photometry is most uncertain redward of about 800 nm (Kalirai et al., 2009), and fringing causes variations in the detected flux of about  $\pm 5\%$  depending on position on the detector (Wong, 2010). We also obtained red and blue images with WFC3 (filters FQ634N and FQ437N) to examine the distribution of chromophores, and compare them with ACS images in filters F658N and F435W.

Methane filter bandpasses for these three instruments are shown in Fig. 2. The WFPC2 filter has a very wide out-of-band blue leak, such that about 40% of the flux in this filter comes from cloud reflectivity outside the methane band (Sromovsky and Fry, 2002). We applied a correction assuming that the flux outside the methane band has the same spatial variation across Jupiter's disk as in a continuum 953-nm filter. Combined with knowledge of the relative throughputs of the two filters, we can subtract the out-of-band flux, leaving an accurate measure of the methane-band reflectivity alone. This technique for correcting the WFPC2 blue leak is described in Lii et al. (2010). The corrected bandpass is very similar to that of the methane filter used in a study of center-to-limb methane-band reflectivity of Oval BE by Sánchez-Lavega et al. (1999), based on 1997–1998 ground-based observations, which

<sup>1</sup> Drizzle, MultiDrizzle, and PyRAF are products of the Space Telescope Science Institute (see Fruchter and Sosey, 2009). Crutil is a package within IRAF (Tody, 1993). Because multiple images of a rapidly rotating spheroid cannot be constructively combined, the added features of MultiDrizzle cannot be used for mosaic composition and cosmic ray cleaning of planetary images. L.A.COSMIC uses Laplacian edge detection to identify cosmic rays (van Dokkum, 2001).

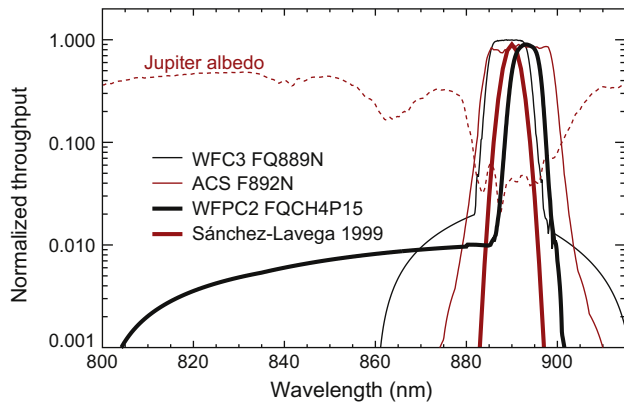


**Fig. 2.** Normalized throughputs in methane filters used by HST WFPC2, HST WFC3/UVIS, HST ACS/HRC, and ground-based Pic-du-Midi observations (Sánchez-Lavega et al., 1999). The logarithmic throughput scale reveals a substantial blue leak in the WFPC2 filter (see text). Dashed line shows Jupiter's full disk albedo spectrum for comparison (from Karkoschka, 1994).

is also shown in Fig. 2. In comparison, the ACS and WFC3 methane band filters are broader, encompassing the wings of the methane band, so data from these instruments give a higher  $I/F$  than for the narrower bandpass data from Sánchez-Lavega et al. (1999) and the corrected WFPC2 data. In Section 4 we show that agreement between the WFPC2 and Sánchez-Lavega et al. (1999) reflectivities demonstrate the accuracy of the blue leak correction technique employed here and in Lii et al. (2010).

Additional WFPC2 issues may lead to small systematic uncertainties. Time variability in WFPC2's photometric sensitivity in the 893-nm filter is described by the ZP\_CORR keyword available in the FITS headers of the calibrated data (Gonzaga and Biretta, 2010). This variability accounts for a  $\sim 4\%$  decrease in total sensitivity from 1994 to 2008, which is smaller than the scatter in our results (Section 4) and neglected in our analysis. A potentially more serious problem is a spectral shift in the central wavelength of the methane filter. Karkoschka and Koekemoer (2002) suggest that this shift varies with position across the filter. Across the filter's complete field of view, they find a 3.3-nm spectral variation, leading to a 29% brightness variation for Jupiter. In our study, Oval BA and its progenitors are located across a much smaller range of detector positions, with a maximum shift of 0.9 nm among the images used (according to the formalism of Karkoschka and Koekemoer, 2002). Under the conservatively naive assumption that brightness variation is linear with spectral shift, this effect would produce an additional uncertainty of  $<8\%$  depending on the positions of the ovals in each data frame. Given the available imaging data, we cannot correct for the spectral shift; a full correction would require measurement of the ovals' spectra in the 890-nm region, obtained for each epoch of imaging data. Instead, brightness variation due to this effect is empirically included in our analysis of the measurement uncertainties, as discussed in Section 4.1.

## 2.2. Velocity field data

Cassini ISS data were used to measure Oval BA's velocity field before the color change. These data were processed as described in Vasavada et al. (2006) and Porco et al. (2003), and image maps were provided by Ashwin Vasavada (2006, private communication). The images were acquired on 12 December 2000, when Cassini was at a distance of about  $1.92 \times 10^7$  km from Jupiter, resulting in 110 km/pixel scale at the location of the oval. The effective image resolution, as determined from the Fourier power spectrum of the images, was 270 km (Asay-Davis et al., 2009). The Cassini data were acquired with the CB2 filter, whose effective

wavelength of 750 nm detects light scattered from clouds throughout the atmospheric column down to pressures greater than 4 bar (Porco et al., 2003; West et al., 2004; Li et al., 2006). The actual pressure level of the cloud features used to track winds within Oval BA has been determined by radiative transfer analyses to be at pressures less than 1 bar: Banfield et al. (1998b) found the cloud sheet to be at  $750 \pm 200$  mbar for Ovals DE and BC, models in Pérez-Hoyos et al. (2009) used a 700 mbar cloud for Oval BA, and the cloud sheet in de Pater et al. (2010b) was at 700–750 mbar. Although Matcheva et al. (2005) extracted zonal average cloud top heights of 700–850 mbar at the latitude of Oval BA from Cassini CIRS spectra, they did not resolve the anticyclone.

Velocities after the color change were made using the ACS/HRC and WFC3/UVIS data described in Section 2.1. Additional HRC images acquired before the color change in January 2005 could not be used for velocity retrievals because Oval BA was less than  $30^\circ$  away from the limb (producing poor feature contrast) and because the maximum time separation of 30 min was too short to provide high precision. The 2006 ACS images (Fig. 1) have a pixel scale of about 90 km/pixel at the location of the oval, with an effective image resolution of 163 km (Asay-Davis et al., 2009). The scale of the 2009 WFC3 images is about 140 km/pixel at the location of the oval.

We have minimized navigation errors by extracting velocities in a frame of reference moving with Oval BA. We accomplished this by shifting images in each set of data with short time separations, so that the retrieved displacements among all possible shifted image pairs are minimized. The shifts applied to the initial frames can be used as an estimate of the navigation errors. For example, the RMS offsets among the 2009 WFC3 image frames were  $0.011^\circ$  in longitude and  $0.054^\circ$  in latitude.

## 3. Horizontal velocities

The best constraints on the dynamics (and changes in the dynamics) of the oval come from examination of the complete velocity field. A thorough assessment requires velocity fields with high accuracy and a high density of velocity vectors. In Section 3.1 we discuss our measurement of the oval's velocity fields in 2000, 2006, and 2009. In Section 3.2 we discuss several distinct characteristics of Oval BA's velocity fields, all of which have implications for the dynamics and structure of the vortex.

### 3.1. Oval BA's velocity fields: measurement

To extract velocities from image sequences of Oval BA, we use the Advection-Corrected Correlation Image Velocimetry (ACCIV) technique, which is thoroughly described in Asay-Davis et al. (2009). Briefly, ACCIV is based on the Correlation Image Velocimetry (CIV) technique, which computes velocities in laboratory flows by tracking passive tracers, accounting for shear and rotation in addition to translation (Fincham and Spedding, 1997; Fincham and Delerce, 2000). In ACCIV, crude initial velocity vector maps (derived with any method) are used to *advect* reflectivity in a pair of images separated by a long time separation to an intermediate time when no real data are available. The difference between the synthetic images at the intermediate time step is iteratively used to generate *correction* vector fields, producing increasingly accurate velocity vectors.

Six radial cuts across the velocity field of Oval BA are shown in Fig. 3, for two Cassini data sets (2000), the ACS/HRC data set (2006), and the WFC3/UVIS data set (2009). These cuts are selected along “spokes” rotated by  $30^\circ$  from each other, and include all velocity vectors within a narrow swath of width  $0.125^\circ$ . The average number of independent velocities in each spoke was 280–290 for the Cassini data sets, 5500 for the ACS data set, and 9100 for the

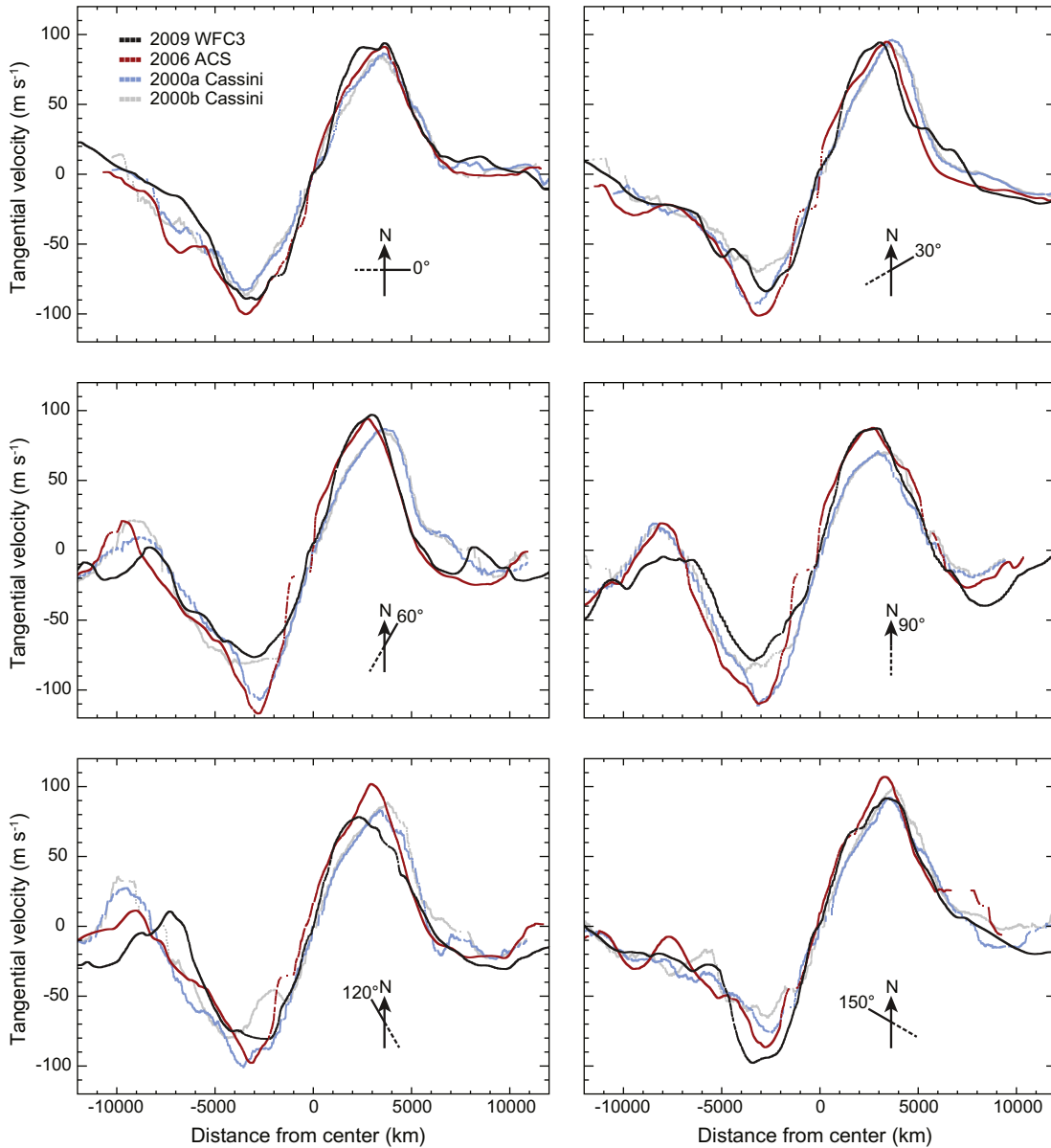


**Fig. 3.** Azimuthal velocities in Oval BA, in 2000, 2006, and 2009, along thin radial “spokes” at  $30^\circ$  intervals and of width  $0.125^\circ$  latitude/longitude. The east–west spoke is at rotation angle  $0^\circ$ ; the north–south spoke is at  $90^\circ$ . Distance ( $x$ -axis) is positive along the solid branch (see compass rose in each panel) and negative along the dashed branch, and velocities are positive clockwise along the solid branch and positive counterclockwise along the dashed branch. Variability between the two Cassini velocity fields—from consecutive rotations—is equivalent to the variability seen from epoch to epoch, so we find no significant changes in Oval BA’s velocity field from 2000–2009. Azimuthal velocities in this plot are perpendicular to the direction of the spokes, rather than tangential to the oval’s elliptical streamlines.

WFC3 data set. Vectors have been smoothed with a moving average for clearer display in Fig. 3; gaps and shelf-like features appear in “bald” patches with low velocity vector density. In general, there are few significant differences among the velocity fields, despite the 2005–2006 color change (specific characteristics of the velocity fields will be discussed in Section 3.2). The primary dynamical boundary of Oval BA is collar of maximum azimuthal velocity, which appears as positive and negative peaks in each “spoke” plotted in Fig. 3. This maximum-velocity collar, at all epochs, lies between about 2500 and 4500 km from the center of the vortex. In Fig. 4, we show the distributions of velocities within the full circumference of the maximum-velocity collar.

Characteristics of the velocities within the collar, including uncertainties, are given in Table 2. We report mean *correlation uncertainties* (an empirical uncertainty estimate defined in Asay-Davis et al., 2009), which range from  $4.8 \text{ m s}^{-1}$  to  $6.9 \text{ m s}^{-1}$  among

the data sets studied. Over the full velocity field inside and outside the collar, the mean uncertainties are 14–36% smaller, but the greatest uncertainties are found with the greatest velocities. The distribution of correlation uncertainties is not sharply peaked and very far from Gaussian, with a long tail extending to about  $20 \text{ m s}^{-1}$ .

Additional systematic uncertainties—due to temporal variation and image quality—may be greater than our quoted correlation uncertainties. They may also be greater than other common methods of estimating uncertainties based on pixel or correlation box size and time separation. In Fig. 3, two Cassini velocity fields are compared, derived from images taken over three consecutive jovian rotations: data from rotations 1 and 2 were used to obtain the 2000a velocity field, and data from rotations 2 and 3 were used to obtain the 2000b velocity field. ACCIV, like other velocity extraction methods in use, relies on the assumption that the velocity field is constant with time. However, the two Cassini velocity fields

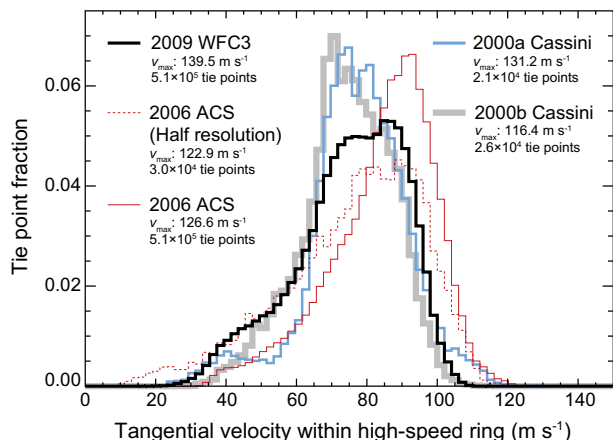


**Fig. 4.** Distribution of speeds over the full circumference of Oval BA's maximum-velocity collar, in 2000, 2006, and 2009. Vertical axis gives the fraction of all vectors within each  $2 \text{ m s}^{-1}$  bin. For this analysis, the maximum-velocity collar was defined as the region between 2500 and 4500 km from the vortex center. Maximum-velocity vectors ( $v_{\text{max}}$ ) do not follow the general variability in the distributions, and are not characteristic of the overall velocity fields. The downsampled ACS data (dashed line) show that resolution effects can broaden the distribution and shift it to lower velocities. Given this systematic uncertainty, there are no changes greater than about  $15 \text{ m s}^{-1}$  in the velocity field of Oval BA between 2000 and 2009.

show differences (mainly near the southern part of the maximum-velocity collar) of  $\sim 40 \text{ m s}^{-1}$ , about four times greater than our estimated uncertainty. It has been previously noted (Asay-Davis et al., 2009; Hueso et al., 2009; Choi et al., 2010; Shetty and Marcus, 2010) that velocities in the northern and southern extremes of the oval's velocity field are strongly affected by Jupiter's zonal jets, and indeed the two consecutive Cassini velocity fields are much more similar in other regions. But these results show that the temporal variation may be active on much smaller timescales than previously recognized, affecting the accuracy of any velocity extraction methods that assume a constant flow field.

Ideally, comparisons should be made between velocity fields extracted from input image data sets sampled at the same spatial resolution. We used maps at  $0.05^\circ/\text{pixel}$  for the ACS and WFC3 retrievals to take advantage of the high pixel resolution of the HST images. For comparison with Cassini maps at resolutions of  $0.1^\circ/\text{pixel}$ , we also extracted velocities from ACS data, downsampled to the same resolution. The two ACS velocity distributions in Fig. 4 show that decreasing the input pixel resolution leads to a broader distribution of velocity values, and a shift to lower speeds. Equivalently, the average velocity in the maximum-velocity collar decreases for input data at lower spatial resolution (Table 2). Although there seems to be a significant increase in mean velocity between 2000 and 2006 based on the full-resolution data, a more appropriate comparison between the 2000 Cassini results with the results using downsampled 2006 data shows no increase in the average velocity in the maximum-velocity collar.

### 3.2. Oval BA's velocity fields: characteristics

Maximum velocities in Oval BA before and after the color change are not good indicators of the overall dynamical state of the vortex, because maximum velocities (by definition) are outliers in the velocity distribution. Other traits—including the size of the maximum-velocity collar, the general distribution of velocities, and radial gradients inside and outside the collar—are more significant.

#### 3.2.1. Maximum velocities

Some of the early published discussion about changes in Oval BA's velocity field centered on changes in the *maximum instantaneous velocities*, which are maximum velocities picked from the whole field, containing additive effects of the vortex component of the flow, the ambient flow (as influenced by the vortex) and turbulence. Increases in Oval BA's maximum instantaneous velocity measured by colleagues after the color change (with stated uncertainties) include  $+25 \pm 83 \text{ m s}^{-1}$  (Simon-Miller et al., 2006b, based on 2001 Cassini and 2006 HST data),  $+28.1 \pm 10\text{--}20 \text{ m s}^{-1}$  (Choi et al., 2010, based on 2001 Cassini and 2007 New Horizons data),  $0 \pm 14 \text{ m s}^{-1}$  (Hueso et al., 2009, based on 2000 Cassini, 2005 and 2006 HST, and 2007 New Horizons data),  $+7 \pm 49 \text{ m s}^{-1}$  (Cheng et al., 2008, based on 2000 Cassini and 2007 New Horizons data).<sup>2</sup>

The disagreement among retrievals, especially among those using common data sets, renders the significance of the changes dubious. Additionally, if we measure changes in the maximum velocity per year, then Table 2 clearly shows that the greatest rate of change in velocity occurred during two consecutive rotations in 2000! The maximum velocity pulled from the entire velocity field at a given epoch is not diagnostic of the overall dynamical state of the vortex—instead, larger characteristics of the entire velocity field should be compared.

#### 3.2.2. Interior radial velocity profile

The radial velocity profiles in Fig. 3 show virtually no change in the radial velocity profile in the interior of Oval BA before and after the color change, agreeing with prior results in Simon-Miller et al. (2006b), Asay-Davis et al. (2009), and Hueso et al. (2009). This means that the relative vorticity did not change. Choi et al. (2010) derived internal radial velocity profiles that were very similar along the east–west axis of the vortex before and after the color change, but showed an increase in the radial velocity gradient along the north–south axis. Their maps also show an increase in vorticity after the color change, but the increase might be explained by the higher resolution of their post-color change data, possibly giving the appearance of a vorticity intensification after the color change. Because resolution effects are significant for velocity fields (Fig. 4), it is likely that there is also a significant effect on vorticities derived from these velocity fields. Because the input resolution of image data is usually not controllable, retrievals based on synthetic data sets may offer a way to test these poorly-constrained systematic effects (Sayanagi et al., 2010).

#### 3.2.3. Boundary changes

Changes in the location and magnitude of the collar of maximum tangential velocity are more difficult to interpret, because they are easily influenced by interactions with the ambient zonal flow. Choi et al. (2010) find significant changes at all intersections of the high-speed collar with the primary (east–west) and secondary (north–south) axes. Positionally, they find a southward shift of the eastward and westward velocity peaks (Fig. 4 in Choi et al. (2010)) by  $1.0\text{--}1.5^\circ$ , a relatively small change given the difficulties of navigating the New Horizons images. They also found intensifications of the maximum eastward, westward, and southward velocities of  $10\text{--}20 \text{ m s}^{-1}$ , and a decrease of maximum northward velocities in the collar of  $7.4 \text{ m s}^{-1}$ . Within their estimated uncertainties of  $10\text{--}20 \text{ m s}^{-1}$ , the Choi et al. (2010) analysis is therefore consistent with the Asay-Davis et al. (2009) and Hueso et al. (2009) findings that the northwards, southwards, and eastwards maximum velocities in the high speed collar did not change

<sup>2</sup> Velocity increases of  $50\text{--}60 \text{ m s}^{-1}$  were reported by Simon-Miller et al. (2006b) and Cheng et al. (2008), but were based on comparisons between velocities in White Oval BC and Red Oval BA; in Asay-Davis et al. (2009) we mistakenly interpreted these velocity increases as pertaining to Oval BA before and after the color change.

**Table 2**  
Velocities within Oval BA's maximum-velocity collar. Absolute magnitudes of velocity vectors (not velocity components tangential to the elliptical envelope) within 2500–4500 km from the center of the vortex were used at each epoch. Mean correlation uncertainty is an estimate of uncertainty described in the text and in Asay-Davis et al. (2009).

Retrieval	Independent velocity vectors	Velocities (m s <sup>-1</sup> )				Mean correlation uncertainty
		Maximum	Mean	Median	Std. dev.	
2009 WFC3	63,900	139.5	76.0	78.0	15.5	6.6
2006 ACS	63,800	126.6	85.6	88.1	14.9	4.8
2006 ACS (Half resolution)	3800	122.9	77.0	80.2	19.8	6.9
2000a Cassini	2600	131.2	78.3	78.9	14.6	6.7
2000b Cassini	3300	116.4	75.5	75.9	12.7	6.2

significantly. All these analyses agree that the maximum westward velocity in the high-speed collar, located at the northern extreme of the vortex, increased by 10–20 m s<sup>-1</sup>, with broad agreement that the change was due to transient interaction with the zonal flow to the north of the oval. Fig. 3 suggests that the transient interaction indeed influenced the 2000 data, because the 2009 data show identical westward speeds to 2006. All studies also agree on a southward shift of this peak, which Hueso et al. (2009) show is also responsible for the shift from triangular to elliptical shapes in the cloud patterns in the exterior of the vortex. Shetty and Marcus (2010) also found that large uncertainties in the Cassini velocity data are concentrated at the northern boundary of the Oval, due to the fact that transients had pulled that boundary into a cusp. Thus, other than distortions related to interactions with zonal jets, no significant changes were found in the size and shape of the dynamical boundary of Oval BA before and after the color change.

### 3.2.4. Cloud coherence time

The cloud coherence time of Oval BA—defined as the length of time over which contrast features remain coherent enough to be identified between separate frames (so that velocities can be extracted)—decreased after the color change, according to Simon-Miller et al. (2006b) and Asay-Davis et al. (2009). These works found coherent, traceable features over 40 min but not over 9 h. Based on the consistent experience between two analyses of the 2006 ACS data, it seemed that the decrease in cloud coherence time could be linked to a change in turbulent velocities, or a change in cloud feature formation and destruction processes within Oval BA.

But the intrinsically subjective nature of cloud coherence time estimates is revealed by our re-analysis of the 2006 data (Figs. 3 and 4), along with the 2009 data: we find that cloud coherence was long enough to perform velocity retrievals over ~10 h at all epochs. We attribute better sets of control parameters (box sizes, spacings, iterations, and smoothing lengths) and improvements to the code for our success in applying ACCIV to the 2006 data, while Asay-Davis et al. (2009) was unable to do so. There are still some regions in the retrieved velocity fields with sparse tie-point coverage; in the cuts shown in Fig. 3, these regions show up as spotty sections or shelf-like horizontal smoothing artifacts. Nevertheless, quantification of overall cloud coherence time is difficult and very sensitive to parameters used in the velocity retrievals. We conclude that cloud coherence is poorly defined and subjectively determined, and previously published discussions of cloud coherence time may need to be viewed cautiously.

### 3.2.5. Exterior radial velocity profile

The velocity field outside the oval's maximum-velocity collar is diagnostic of the static stability of the atmosphere in the environment of jovian anticyclones (Shetty et al., 2007; Legarreta and Sánchez-Lavega, 2008). Shetty and Marcus (2010) modeled the decay of tangential velocity outside Oval BA, from the maximum-velocity

collar outwards to the zonal background flow, and found that the lack of change in this characteristic in the 2000 Cassini and 2006 HST velocity fields (Asay-Davis et al., 2009) implied that the static stability in the oval's environment was identical to within the ~10% stated uncertainties at both epochs. These conclusions were drawn based on a quasigeostrophic 1.5-layer model with no parameterization of vertically varying static stability; these findings are further discussed in Section 5.2. The 2009 velocity field in the immediate exterior of the vortex is also indistinguishable from prior measurements, within the uncertainties (Fig. 3). The exterior radial velocity profile is an important trait, and its lack of change before and after the color change is one of the key parameters in the modeling studies (Shetty and Marcus, 2010) central to Sections 5.2.2 and 5.3.

## 4. Tropospheric haze

The tropospheric haze atop Oval BA relates to the vertical structure of the vortex, to the dynamics controlling the vertical mixing, and potentially to photochemical processes involving chromophores. We analyze two properties of the tropospheric haze that are particularly relevant to the color change of the oval: the variation of the haze opacity over time, and the correlation between the horizontal distributions of the haze, of the red coloration, and of the velocity field.

### 4.1. Haze temporal variation

In imaging data, the reflectivity of the tropospheric haze above the oval (and its progenitors) depends on the incident and emission angles at the position of the oval in each frame. This geometric effect must be removed before temporal variation can be studied. At each epoch of Hubble observations, we sampled the reflectivity with an ellipse centered on the ovals, with a longitudinal width of 3° and a latitudinal width of 2.2° (smaller than the area of uniform haze enhancement atop each oval). Each frame of data was reduced to a pair of values: mean  $I/F$ , and root-mean-square  $I/F$  variation within the sampled region. Fig. 5 shows reflectivities derived from each frame of the sampled WFPC2  $I/F$  data, plotted as a function of the cosine of the incident light angle ( $\mu_0$ ). A linear fit to the complete data set gives a slope (in non-dimensional units of  $I/F/\mu_0$ ) of  $0.149 \pm 0.002$ . We used this fit to extrapolate the reflectivity of the oval to  $\mu_0 = 0.84$ , which corresponds to a location on the central meridian at 33° latitude (with a subsolar latitude of 0°). This correction is proportional to a Minnaert correction for photometric variation due to illumination and viewing geometry of the form  $\mu_0^k \mu^k$ , where  $\mu$  is the cosine of the emission angle and  $k = 1$ . All latitudes are expressed as planetographic coordinates in this work.

The average of all WFPC2 frames per epoch after correction for viewing geometry (i.e., the central meridian  $I/F$  of the ovals) is plotted in Fig. 6 using black symbols. Error bars represent combined uncertainties from the geometric correction, calibration, and

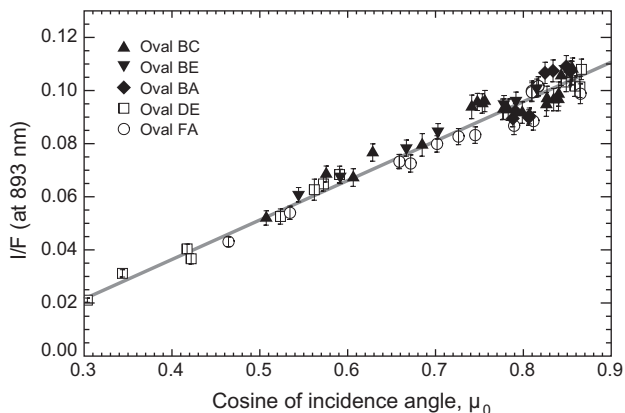


**Fig. 5.** Methane-band reflectivity of jovian anticyclones as a function of the cosine of the incidence angle. Each symbol corresponds to a single frame of WFPC2 imaging data acquired between 1995 and 2008, with error bars representing the standard deviation of reflectivity among pixels sampled near the center of the anticyclone. Data fall along a line with slope of  $0.147 \pm 0.005$ .

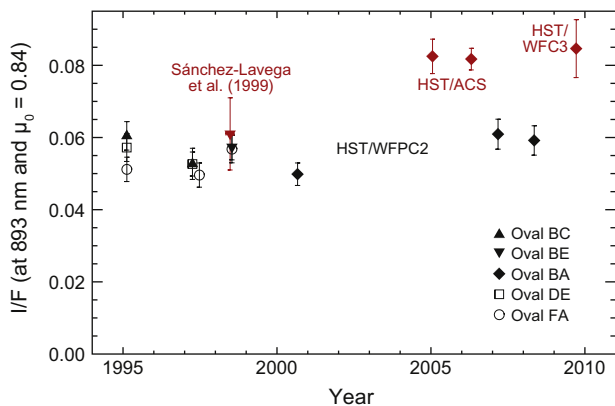


**Fig. 6.** The ovals' reflectivity as a function of time. Symbol shapes distinguish between the Oval BA and its predecessors, with WFPC2 observations in black (after correction for the methane filter blue leak). Shaded symbols correspond to ground-based Pic-du-Midi observations (Sánchez-Lavega et al., 1999) in 1998, HST ACS/HRC observations in 2005 and 2006, and HST WFC3/UVIS observations in 2009. Each point is an average of reflectivities acquired at a single epoch of observation. To remove effects of viewing geometry, the reflectivity in each frame was projected to a value of  $\mu_0 = 0.84$  (corresponding to the location of the ovals on the central meridian, for a subsolar latitude of  $0^\circ$ ) prior to averaging. Error bars represent combined uncertainties in this geometric correction, as well as calibration uncertainties and variability within each epoch of observations (including possible effects of shifts in the filter's central wavelength described in Karkoschka and Koekemoer, 2002).

variability between multiple frames at a single epoch, which empirically includes any variability due to central wavelength shifts as a function of position on the WFPC2 methane-band filter (Karkoschka and Koekemoer, 2002). The WFPC2 data in 2007 and 2008 (after the color change) indicate a haze reflectivity that is statistically identical to the mean central meridian reflectivity of  $0.055 \pm 0.004$ . The 1998 WFPC2 data, after correction for the blue leak (Section 2.1), agree with the Oval BE central meridian methane-band reflectivity of  $0.063 \pm 0.010$  reported by Sánchez-Lavega et al. (1999) based on measurements taken at Pic-du-Midi in 1998.

The WFPC2 data set shows that the opacity of the tropospheric haze atop Oval BA and its progenitors has remained stable over the 13-year span of the data set. This data set has both advantages and disadvantages. Using data from a single detector avoids photometric uncertainties arising from intercomparison of data from differ-

ent sources, assuming the detector and filters are sufficiently monitored for changes over time. The long lifetime of WFPC2 allows a study of the vortices before and after the mergers of Ovals BC, BE, DE, and FA, and before and after the color change of Oval BA. Although these imaging data are ideal for observing long-term variation, they cannot resolve the degeneracy between the vertical structure and the total opacity of the haze. To give a sense of this degeneracy, Pérez-Hoyos et al. (2009) showed that the same reflectivity can be matched with a haze layer extending up to 100 mbar with a total optical depth of 2, or extending only to 350 mbar with a total optical depth of 10. Spectroscopy or multi-wavelength imaging (Banfield et al., 1998a, 1998b; de Pater et al., 2010a, 2010b) are superior for constraining haze density and vertical structure, but we instead use the WFPC2 imaging data because a long-term spectroscopic record of the methane-band reflectivity of these features is simply not available.

Data from the other HST instruments that imaged Oval BA in the 890-nm methane band—ACS and WFC3—are also shown in Fig. 6, as shaded diamonds. Empirical corrections have also been made to these data for viewing geometry, with the same form as for the WFPC2 data but with slopes of  $0.110 I/F/\mu_0$  (WFC3) and  $0.126 I/F/\mu_0$  (ACS). The ACS data are particularly useful because they are the highest resolution imaging data closest in time to the color change. They show that haze reflectivity was the same at both epochs, to well within the uncertainties. Qualitatively, Simon-Miller et al. (2006b) also used these ACS data to show that the appearance of Oval BA was different only in the blue (435 nm) filter. Pérez-Hoyos et al. (2009) used these same ACS data, in combination with data in five other filters, to constrain radiative transfer models of the oval and show that its haze layer was unchanged before and after the color change. Their much more comprehensive analysis broke the degeneracy between haze top height and haze optical thickness. With this more direct approach, they found that the height of the haze had not changed before and after the color change. Combined with the results of Pérez-Hoyos et al. (2009), Fig. 6 suggests that the altitude of the top of the haze above Oval BA and its progenitors was roughly constant between 1995 and 2008.

Due to the different bandpasses shown in Fig. 2, it is difficult to directly compare the WFC3 data with the other data sets, although the 2009 WFC3 reflectivity of  $0.085 \pm 0.001$  is consistent with the ACS values of  $0.083 \pm 0.005$  and  $0.082 \pm 0.003$  for 2005 and 2006, respectively. The WFPC2 data set shows the value of a single instrument with over a decade of service; hopefully the WFC3 data point is the first of many to come in the era after Hubble's fourth and final scheduled servicing mission in 2009.

#### 4.2. Haze distribution

The collar of maximum-velocity winds, indicated as a dotted ellipse in each frame of Fig. 7, almost perfectly confines both the haze and the chromophores. Results based on multi-spectral imaging data from the Galileo Orbiter (Simon-Miller et al., 2001) found that Jupiter's chromophores were generally confined to the upper tropospheric haze, rather than the thicker underlying cloud layer. High altitude chromophores are also suggested by the strong correlation between haze and coloration in Fig. 7.

The tight overlap between the haze and dynamical boundaries agrees with the vortex secondary circulation scheme described in de Pater et al. (2010b), Marcus et al. (2011), and Section 5.1, which features air rising along the central axis of the vortex. The elevated upper tropospheric haze layer may mean that the vertical velocity associated with this circulation is greater than the precipitation speed of haze particles above the vortex, and that the more adiabatic lapse rate within the vortex (compared with the surroundings) enables faster diffusive mixing within the vortex (generally

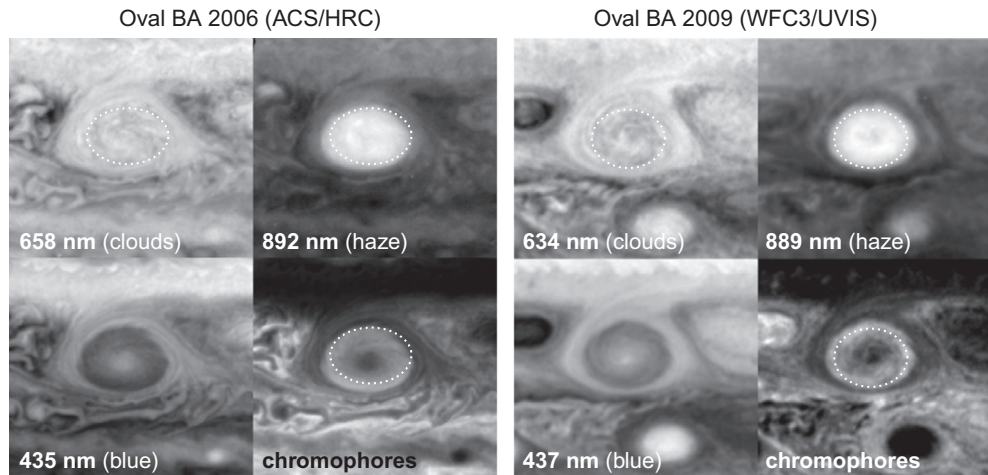


**Fig. 7.** Chromophore and tropospheric haze distributions of Oval BA, using HST data from 2006 (left) and 2009 (right). Dashed line indicates the approximate location of the collar of maximum azimuthal velocity, which forms the dynamical border of Oval BA. Haze and chromophores appear to be confined within this dynamical border. Chromophore panel is a map of  $1 - (F435N/F658N)$ , which normalizes color difference by red reflectivity, in order to remove the effect of spatially-variable cloud opacity. A very similar color gradient from the core to the edge of the oval is present at both epochs. The core-to-edge I/F contrast in the blue filters is about 20% at both epochs, although the 2009 image scaling is biased due to the dark red cyclone just to the west of Oval BA.

consistent with greater eddy mixing at the top of the GRS compared to similar latitudes in Edgington et al., 1999).

## 5. Vertical structure of Oval BA

Oval BA's velocity fields, and the history of its haze reflectivity variation, relate to the vertical structure of the vortex. To interpret these observations, we describe the thermodynamic structure (temperature, pressure, and density as a function of position) of Oval BA. Observable vortex characteristics are sensitive to the static stability in the fluid surrounding the vortex, according to numerical and laboratory experiments. A key difference between the experiments and Jupiter's atmosphere is that static stability varies with altitude in Jupiter, but is taken to be constant in experiments to date. But by taking the vertical variation of static stability into account, we extend the experimental results to estimate the vertical extent of the vortex.

This section reviews published work concerning Oval BA's thermodynamic structure (Section 5.1), the static stability in Jupiter's atmosphere (Section 5.2.1), and the static stability of the vortex environment based on numerical and laboratory experiments (Section 5.2.2). Our review of these prior findings is then used to support new conclusions in Section 5.3: that static stability can be used like a measuring stick to determine the height of the vortex, that the oval's height was unchanged before and after the color change, and that the vortex extends down to the condensation level of water in supersolar abundance.

### 5.1. Thermodynamic structure of Oval BA

Fig. 8 shows the key thermodynamic features of anticyclonic jovian vortices like Oval BA: a high-pressure center, sandwiched by a cold and dense top and a warm and buoyant bottom. Observational and modeling results strongly support the cold lid and high-pressure center. A warm and buoyant bottom is also expected based on the secondary circulation depicted, although cloud obscuration prevents thermal anomalies from being measured beneath the large jovian anticyclones.

As an anticyclone, Oval BA must possess a central high-pressure anomaly. Around this high pressure anomaly, tangential winds experience a balance between the pressure force and the Coriolis force, in a primary flow that can be characterized by its Rossby

number  $R_0 = V/(L|f|)$ , where  $f$  is the Coriolis parameter and  $V$  and  $L$  are the oval's characteristic velocity and length (Pedlosky, 1987; Kundu, 1990). Fig. 4 yields estimates of  $V = 80$  m/s and  $L = 3500$  km, the Coriolis parameter at the latitude of Oval BA is  $-1.9 \times 10^{-4} \text{ s}^{-1}$ , so the oval's Rossby number is about 0.12. For  $R_0 \ll 1$ , the flow is in geostrophic balance. This flow is the primary circulation of the vortex, shown in Fig. 8 as counterclockwise arrows measured at the cloud deck. The lack of change in Oval BA's horizontal wind field (Section 3) thus implies that its high pressure anomaly did not change between 2000 and 2009.

A commonly accepted rule of thumb holds that upper tropospheric low temperature anomalies can be used to identify cloud features as anticyclonic (e.g., Cheng et al., 2008). Flasar et al. (1981) assert that rising motion and adiabatic cooling are responsible for the cold anomaly over the Great Red Spot observed by IRIS, and predict a warm core beneath the high-pressure centers of such anticyclones. A system with return flow outside the vortex (as in Flasar et al., 1981 and Conrath et al., 1981) is similar to Ekman circulation (Kundu, 1990), in that angular momentum is exchanged with the surroundings, there is frictional damping at the top and/or bottom boundary, and the vortex spins down quickly.

The circulation in Fig. 8 differs from the Conrath et al. (1981) scenario in that the return flow is within the vortex, and that radiative dissipation rather than frictional damping drives the secondary circulation. In smaller vortices, this return flow creates clearings in the cloud layers at the outer vortex edge and rings of high  $5\text{-}\mu\text{m}$  radiance, but in larger vortices like Oval BA and the Northern Red Oval at  $42^\circ\text{N}$ , the return flow occurs within the cloudy area of the vortex and does not clear out the cloud layers (de Pater et al., 2010b, 2011). The scale analysis of this secondary circulation is new in that it features radial velocities on the order of  $1 \text{ m s}^{-1}$  and vertical velocities on the order of  $2 \text{ cm s}^{-1}$  (de Pater et al., 2010b). The secondary circulation in the upper part of the Oval BA transports anomalous density upward (and a flux of anomalous entropy downward) near the central axis of the vortex. This transport maintains the cold anomaly at the top of Oval BA (and a warm anomaly at the bottom) and also creates a temperature profile all along the central axis of the vortex that is closer to the adiabatic lapse rate than the profile in the surrounding atmosphere. This secondary circulation scheme also predicts a relation between the vortex aspect ratio and the static stability of the environment that is verified by laboratory experiments (Aubert, 2010; Aubert et al., 2010).

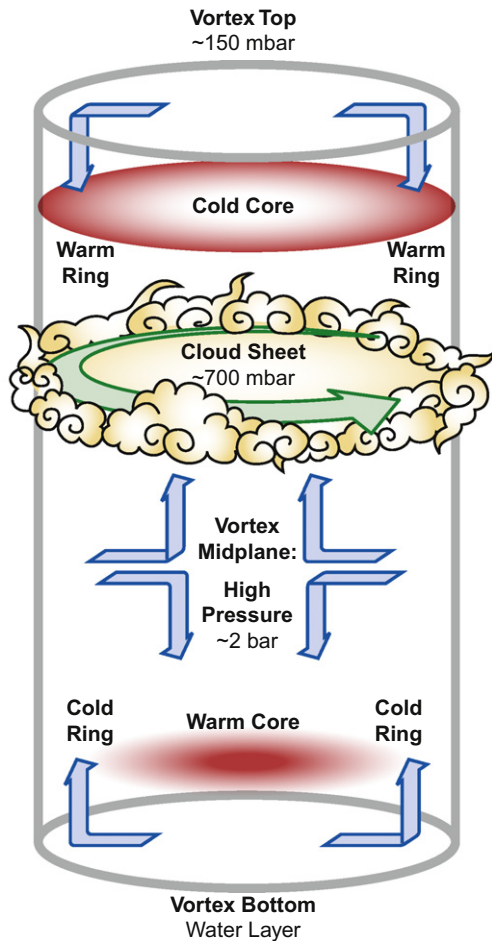


**Fig. 8.** Vortex structure and circulation. Primary circulation is counterclockwise as measured at the cloud sheet, near the vortex midplane. Secondary circulation is shown by arrows with vertical components. Thermodynamic anomalies (the cold core and warm core) are depicted near the top and bottom of the vortex. The circulation differs from the Conrath et al. (1981) model in that the return circulation is inside the vortex, and that frictional dissipation (as in Ekman pumping) is not required. Estimates for pressures at the vortex top and cloud sheet are from radiative transfer analyses reviewed in Sections 2.1 and 2.2. Estimate for the vortex midplane pressure follows the scaling analysis in de Pater et al. (2010b). Evidence that the vortex bottom extends to the water layer is discussed in Section 5.2.2.

The secondary circulation and its scaling analysis are consistent with a wide range of published observations of dynamical tracers: temperature, para hydrogen fraction, and concentrations of ammonia and phosphine. Ground-based thermal infrared observations have recently begun resolving features on the scale of large anticyclones like Oval BA. Observed temperature contrasts for both Oval BA (Cheng et al., 2008) and the GRS (Fletcher et al., 2010) were about 3 K from the cores to the dynamical boundary of the vortices. However, assuming diffraction-limited resolution at 13–20  $\mu\text{m}$  for the VLT data presented in Cheng et al. (2008), Oval BA is only 3–5 resolution elements across. The actual temperature contrast between the coldest and warmest parts of the oval could therefore plausibly be up to 5 K, considering unresolved structure.

Other dynamical tracers derived from ground-based observations qualitatively support a circulation scheme with uprising air along the vortex core and radial spreading at the top of the vortex. Fletcher et al. (2010) reported significantly lower para-hydrogen fractions at 100–400 mbar in the GRS as compared to outside the GRS. Over timescales on the order of 10 years, ortho- and para-hydrogen in the upper troposphere will equilibrate to higher para-hydrogen fractions (Massie and Hunten, 1982; Conrath and

Gierasch, 1984). The low para-hydrogen anomaly reported by Fletcher et al. (2010) within the GRS provides a limit that the timescale of mixing within that anticyclone is shorter than about 10 years. For Oval BA, de Pater et al. (2010b) apply a scaling analysis to the secondary circulation scheme in Fig. 8 to derive a mixing timescale on the order of months, well within the limit imposed by para hydrogen fraction measurements.

Ammonia concentration can also be useful as a dynamical tracer, and spectroscopic studies of the Great Red Spot suggest a complex variation of ammonia concentration as a function of height within that vortex (e.g., Tokunaga et al., 1980; Griffith et al., 1992; Edgington et al., 1999; Achterberg et al., 2006). Cheng et al. (2008) demonstrated the ability to resolve Oval BA and an adjacent cyclonic feature using the Very Large Telescope at 10.77  $\mu\text{m}$ , where ammonia concentration modulates the outgoing flux, but the smaller size of Oval BA and its progenitors rendered them unresolved to prior investigations. Improvements in ground-based facilities will hopefully lead to new measurements constraining the spatial and temporal variation of ammonia concentration in and around Oval BA.

Simulations also produce the cold and dense anomaly atop anticyclones. In a numerical simulation using the OPUS GCM, a cold anomaly of about  $-0.12$  K was found above a transient vortex at about  $33^\circ\text{S}$  (Zuchowski et al., 2009). This anomaly is much smaller than the  $\sim 3$  K contrast between Oval BA and its surroundings in Cheng et al. (2008), possibly because the vortex in the numerical simulation was transient rather than a steady-state phenomenon. Another numerical simulation, constrained by laboratory experiments with a stratified fluid in a rotating tank, also found a dense lid atop the vortex, but in this case after the vortex had equilibrated (Aubert, 2010).

## 5.2. Static stability and vortex vertical scale

Modeling results show that vortex velocity fields are sensitive to the static stability of the surrounding atmosphere (Shetty et al., 2007; Legarreta and Sánchez-Lavega, 2008; Shetty and Marcus, 2010). Modeling studies typically assume a constant static stability with depth in the troposphere (Section 5.2.2). However, there is both observational and theoretical evidence that Jupiter's static stability actually varies with depth (Section 5.2.1). Cloud formation is the source of this stratification, via release of latent heat and compositional gradients.

Static stability can be discussed in terms of  $N$  (the Brunt–Väisälä frequency),  $L_R$  (the Rossby deformation radius), or a deviation from the dry adiabatic lapse rate:

$$N = \frac{|f|L_R}{H} = \sqrt{\frac{g}{T} \left( \frac{dT}{dz} + \Gamma_{ad} \right)} \quad (1)$$

where  $|f|$  is the magnitude of the Coriolis parameter at the latitude of interest (ranging from  $1.8$  to  $2.0 \times 10^{-4} \text{ s}^{-1}$  across the semiminor axis of Oval BA,  $1.0$  to  $1.5 \times 10^{-4} \text{ s}^{-1}$  for the GRS),  $\bar{H}$  is the scale height of the atmosphere (about 60 km at 15 bar, decreasing to about 20 km at pressures less than 1 bar),  $g$  is the effective gravitational acceleration,  $T$  is the temperature in Kelvin, and  $\Gamma_{ad}$  is the dry adiabatic lapse rate (defined to be positive). In the discussion of jovian static stability estimates below, values have been converted to  $N$  in cases where they were reported as other quantities. At  $33^\circ\text{S}$  for example, a value of  $N = 0.01 \text{ s}^{-1}$  corresponds to  $L_R = 1000$  km and  $dT/dz + \Gamma_{ad} = 0.6 \text{ K}$  at 0.5 bar, or  $L_R = 2100$  km and  $dT/dz + \Gamma_{ad} = 1.2 \text{ K}$  at 5 bar.

### 5.2.1. Observations and simulations of layered stability

Observations and simulations of static stability in Jupiter's atmosphere agree that it is variable with altitude. In Fig. 9, we

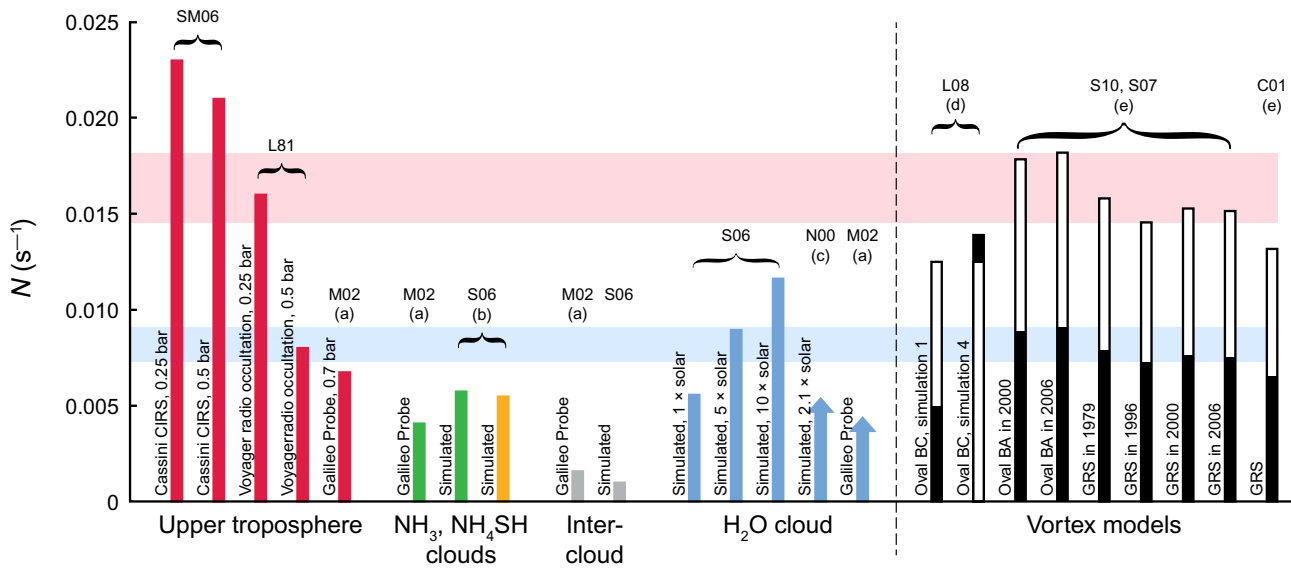


**Fig. 9.** Estimates of static stability in Jupiter's atmosphere. Shaded bars (to the left of the dashed line) are from measurements and models of Jupiter's vertical structure; black and white bars (to the right of the dashed line) are for vortex surroundings as determined by numerical models of the GRS, Oval BA, and the progenitor Oval BC. At the left, results are grouped into regions: top of the troposphere, in the cloud decks, and between clouds. Lower horizontal band shows that values of  $N$  derived from vortex models for the deep atmosphere (black bars) are consistent with static stability from supersolar water condensation. Upper horizontal band shows that  $N$  derived from vortex models for the upper atmosphere (white bars) are consistent with static stability measured in the upper troposphere. Where static stability values were originally reported as deviations from the adiabatic lapse rate or as the Rossby deformation radius, they have been converted to Brunt–Väisälä frequency  $N$  as described in the text and in Eq. (1). Sources and notes: SM06 = static stability derived from Cassini CIRS temperature profiles in Simon-Miller et al. (2006a). L81 = static stability derived from Voyager radio occultation data in Lindal et al. (1981). M02 = static stability measured by Galileo Probe ASI from Magalhães et al. (2002). S06 = theoretical static stability due to cloud condensation models in Sugiyama et al. (2006). N00 = static stability from 2D convective model in Nakajima et al. (2000). S07 and S10 = static stability from 3D hydrodynamic vortex simulations in Shetty et al. (2007) and Shetty and Marcus (2010). C01 = quasigeostrophic model of Cho et al. (2001) as constrained by Voyager cloud morphology. (a) We assign Magalhães et al. (2002) values to cloud and inter-cloud levels by using the scaling correction for 5- $\mu\text{m}$  hot spot meteorology from Wong (2009). Value for water cloud is a lower limit because the probe probably did not reach levels corresponding to the base of the water cloud. (b) Used 5 $\times$  solar (Grevesse et al., 2007) condensable volatile abundances. (c) Strong forcing in this simulation may lead to an overestimate of the humidity above 5 bar, equivalent to an underestimate of the static stability near the water cloud base. (d) Cases 1 and 4 are minimum and maximum values of  $N$  (black bars) tested in models of Legarreta and Sánchez-Lavega (2008) for the 5-bar level; white bars give  $N$  at 0.5 bars in these same cases. (e) Vertically averaged Rossby deformation radius was converted to  $N$  at the latitude of Oval BA and at pressure levels of 0.5 bar (white bars) and 5 bar (black bars) using Eq. (1), with  $H = 20$  km at 0.5 bar and  $H = 40$  km at 5 bar.

summarize static stability estimates from different sources and at different altitude levels (shaded bars; left half). In the upper troposphere (far left of Fig. 9), stability is greater than at deeper levels. At 250 mbar, which is near the top of Oval BA, the temperature profile derived from Voyager radio occultations (Lindal et al., 1981) gives a Brunt–Väisälä frequency of about  $N = 0.015 \text{ s}^{-1}$ ; at the same pressure level, Simon-Miller et al. (2006a) derive temperature profiles from Cassini CIRS spectra that result in even higher values of  $0.023 \text{ s}^{-1}$  at Oval BA's latitude. Deeper (at 500–700 mbar), both the Voyager radio occultation data and Galileo Probe *in situ* data find  $N = 0.007\text{--}0.008 \text{ s}^{-1}$ . The 500-mbar static stability from Cassini CIRS is again higher at  $N = 0.021 \text{ s}^{-1}$ , although at such high pressures temperature uncertainties are high due to the influence of aerosols on the spectrum (Simon-Miller et al., 2006a).

The deepest atmospheric structure measurements from remote sensing are the Voyager radio occultation results, which found an adiabatic profile (to within  $\pm 0.2 \text{ K km}^{-1}$ , corresponding to  $N = 0.006 \text{ s}^{-1}$  or lower), down to about 1 bar. Below this level, static stability has been measured only by the Galileo Probe (Seiff et al., 1998; Magalhães et al., 2002), at a latitude of  $7.5^\circ\text{N}$  (Young, 2003). The Galileo Probe measurements fit within the Voyager  $\pm 0.2 \text{ K km}^{-1}$  uncertainty envelope, but have much lower uncertainties of about  $0.05 \text{ K km}^{-1}$  (Magalhães et al., 2002).

The probe profile is characterized by three stable layers of  $N \geq 0.004 \text{ s}^{-1}$ , with two intervening adiabatic neutral zones. To relate stratification in the probe entry site to stratification in the general jovian environment, we must take into account the peculiar meteorology encountered by the Galileo Probe as it entered a 5- $\mu\text{m}$  hot spot (Orton et al., 1998). Models of 5- $\mu\text{m}$  hot spots as non-

linear planetary wave phenomena (Friedson, 2005; Showman and Dowling, 2000) explain how “normal” jovian air is vertically displaced upon entering 5- $\mu\text{m}$  hot spots, so we compensate for the displacement by reassigning the probe's static stability measurements (Magalhães et al., 2002) to lower pressures (higher altitudes) in Fig. 9. This empirical remapping is based on two independent observational signatures that mark the levels where clouds condense: peaks in stability, and “equilibration levels” at which condensable gas mixing ratios reach their deep values. Mixing ratios of  $\text{NH}_3$  and  $\text{H}_2\text{S}$  increased with pressure in the probe entry site, until they reached equilibration levels of about 8 and 12 bar respectively; below the equilibration level of each gas, its mixing ratio remained constant with depth (Niemann et al., 1998; Wong et al., 2004). As discussed in greater detail in Wong (2009), the remarkable coincidence between the stable layers and the equilibration levels provides additional support to the idea that the Galileo Probe descended through compositional and thermodynamic fossils of jovian cloud layers (e.g., Atreya et al., 1997; Showman and Ingersoll, 1998; Young, 2003).

The values of  $N$  for the stable layers in simulations are consistent with the Galileo Probe measurements. Sugiyama et al. (2006) used an equilibrium cloud condensation model to find that latent heat release and molecular weight variation combined to create stable layers of  $N \sim 0.006\text{--}0.012 \text{ s}^{-1}$ , corresponding to the  $\text{NH}_3$ ,  $\text{NH}_4\text{SH}$ , and  $\text{H}_2\text{O}$  clouds. Between the clouds, the atmosphere approached neutral stability, with  $N \sim 0.001 \text{ s}^{-1}$ . These static stability estimates are labeled “S06” in Fig. 9, with values that closely match Galileo Probe results. This type of model predicts a very idealized atmospheric column, with maximum condensation at every

atmospheric level. To include the effects of dynamics, Nakajima et al. (2000) instead used a two-dimensional hydrodynamic model, finding a persistent stable layer near the base of the water cloud resulting from moist convection. The water cloud layer in this model had weaker stability than in the equilibrium cloud condensation case, but Nakajima et al. (2000) noted that the accelerated timescale in their simulations may underestimate stability in Jupiter's atmosphere. Thus, we mark the water layer stability from this model (labeled "N00" in Fig. 9) as a lower limit.

No prior work has collectively compared the observational and theoretical results shown in Fig. 9, which demonstrates that the vertical variation of static stability in Jupiter's atmosphere is reasonably well understood. Of course, the temporal and meridional variation of static stability is unconstrained by the simulations and observations, but vortex modeling can at least address temporal variation of static stability at the latitude of Oval BA.

### 5.2.2. Static stability in the vortex environment

Stratification derived from vortex models is summarized in Fig. 9 (black and white bars; right half). In each case, white bars are upper tropospheric static stability, and black bars are lower tropospheric (5–7 bar) static stability. Static stability varies with altitude for different reasons in each model.

Legarreta and Sánchez-Lavega (2008) modeled Oval BC using the EPIC code, testing several cases with different static stability profiles. They found reasonable behavior for  $N$  between 0.005 and  $0.014 \text{ s}^{-1}$  in the 3–7 bar region (black bars marked "L08" in Fig. 9), and  $N \sim 0.0125 \text{ s}^{-1}$  at 0.5 bar (white bars). A more precise constraint on static stability was not available because computational limitations permitted only a sparse coverage of the input parameter space.

Other vortex simulations—by Shetty et al. (2007), Shetty and Marcus (2010), and Cho et al. (2001)—did not model vertical variation of static stability, which was reported only as a single value of  $L_R$  for each case. Because the atmospheric scale height is proportional to temperature, translating the reported  $L_R$  to  $N$  using Eq. (1) results in larger values for the upper troposphere (white bars labeled "S10", "S07" and "C01") than for the deep atmosphere (black bars). Values from Shetty et al. (2007) and Shetty and Marcus (2010) are perhaps the most precise, with stated uncertainties of 10%, based on equilibrium solutions of the quasi-geostrophic equations of motion constrained by 2000 and 2006 velocity fields of Oval BA. The low uncertainties result from parameter selection by a genetic algorithm that searched hundreds of thousands of cases. The value of  $N$  found by Cho et al. (2001), based on modeling GRS cloud morphology in Voyager imaging data, has a stated accuracy of a factor of two.

The lower horizontal band in Fig. 9 spans the deep tropospheric values from Shetty and Marcus (2010) and Shetty et al. (2007), and the higher band spans the upper tropospheric values from these works. The results from vortex models in Cho et al. (2001) are close to these horizontal bands, and the deep values from Legarreta and Sánchez-Lavega (2008) bracket the deep values retrieved from Shetty and Marcus (2010) and Shetty et al. (2007). Thus, there is broad agreement among models that static stability is near the upper band in the upper troposphere, and near the lower band in the lower troposphere. The upper band intersects upper tropospheric measurements from Cassini CIRS and the Voyager radio occultations, giving confidence to the sensitivity of vortex models to static stability. In the deeper troposphere, the vortex models retrieve static stability values that are consistent with a supersolar water cloud layer, but too large to be consistent with clouds of solar water abundance,  $\text{NH}_3$ , or  $\text{NH}_4\text{SH}$ .

### 5.3. Summary: Oval BA's vertical structure unchanged

The comparison of vortex models with estimates of vertical variation of static stability leads to two profound results: that the

large jovian anticyclones must extend down to the water cloud, and that Jupiter's water abundance is supersolar. The extension of Oval BA and the GRS down to the water cloud layer is roughly consistent with the half height of the oval, 60 km, from the scaling analysis in de Pater et al. (2010b), as well as the range of 1–5 scale heights explored in Legarreta and Sánchez-Lavega (2008). Additionally, thin 5- $\mu\text{m}$  bright arcs are visible to the south of the GRS in Keck data from 2006, and to the south of Oval BA in both 2006 and 2008 (de Pater et al., 2010b). Although the dynamics of the arcs are not known, their persistence and conformity with the azimuthal velocity profiles of the vortices suggest that the arcs are closely associated with the vortices, and therefore the vertical depth of the arcs (5 bar or more based on their 5- $\mu\text{m}$  radiance) is indicative of the vertical depth of the vortices. A precise constraint on the pressure level at the bases of the vortices, based on static stability derived from dynamical models, cannot be made at this time due to uncertainties in the stability at the water condensation level. Equilibrium condensation models give an upper limit on the stability generated by water condensation, but dynamics in Jupiter's atmosphere can result in lower amounts of static stability for nearly the same water abundance (Nakajima et al., 2000).

The available data constrain the amount of change to Oval BA's thermodynamic structure, and to the static stability of the ambient atmosphere. Static stability varies with altitude, so the lack of variation in the static stability determined by models implies that the oval reached the same pressure levels at its upper and lower boundaries, before and after the color change. Additionally, models constrained by cloud morphology in Cho et al. (2001) indicate that the stability was constant to within a factor of two, since no significant morphological changes are seen in Oval BA's clouds (Simon-Miller et al., 2006b).

## 6. Discussion

The color change of Oval BA implies some change in underlying physical properties of the oval. Phenomenologically, Pérez-Hoyos et al. (2009) demonstrated that the primary change is described by an increase of blue absorption among the aerosols in the oval—in terms of a decrease of the imaginary index of refraction or of the single scattering albedo—but this does not illuminate the underlying physical causes responsible for the change in particle properties. We discuss the possibility that the color change of Oval BA is related to an increase in temperature of the surrounding atmosphere, which would affect chromophore processes (photochemical production or mantling) within the oval. An alternative possibility, that dredging became faster or reached deeper, is not as compelling.

### 6.1. Chromophores and chromophore processes

In 1986, West et al. extensively reviewed the composition of jovian chromophores, and in the subsequent 25 years only limited progress has been made in that area. That paper reviewed the photochemical production of red particulates, with the most plausible pathways beginning with photolysis of  $\text{PH}_3$  or  $\text{NH}_4\text{SH}$  in the upper troposphere. Baines et al. (2004) and Delitsky and Baines (2007) reported progress on modeling production of chromophores by gas-phase reactions between species produced by the irradiation of  $\text{NH}_4\text{SH}$ . Because both phosphorous- and sulfur-based red solids have very broad absorptions in the blue region of the visible spectrum, compositional identification of the chromophores by remote sensing is difficult, but observers are stepping up to this challenge: a preliminary report (Strycker et al., 2006) suggested that visible spectra favor polyatomic phosphorous compositions.

Chromophores are most likely thermochemically stable or meta-stable; they are well mixed possibly as deep as 2 bar

(West et al., 1986), where temperatures exceed 200 K (Seiff et al., 1998). This stability implies that a change in chromophore destruction rates is unlikely. Production rates would increase if there were a change in supply rates for chromophore precursors, by dredging for example. A temperature change might also affect production rates, because photochemical chromophore production could involve a series of gas-phase reactions, possibly with strong temperature dependences. A tabulation of chemical reactions relevant to the lower atmosphere of Venus (Krasnopolsky, 2007) includes 14 temperature sensitive reactions involving sulfur and hydrogen atoms. The most temperature-sensitive of these reactions, involving elemental sulfur, have rates that change by a factor of  $\sim 10^7$  in response to a temperature change of about 5 K in Jupiter's upper troposphere. Pérez-Hoyos et al. (2009) also suggest that the color change is related to photochemical transformation of chromophore precursor materials in the upper troposphere. But the role of gas-phase chemistry is unclear, since ultraviolet irradiation of solid  $\text{NH}_4\text{SH}$  at  $\lambda < 300$  nm changes its color from white to yellow (Sill, 1973; Lebofsky and Fegley, 1976). This process is feasible since observations (Sromovsky and Fry, 2010) and simulations (Sugiyama et al., 2009) are consistent with the presence of  $\text{NH}_4\text{SH}$  at the cloud tops.

If a change in chromophore production rate is not the underlying cause for Oval BA's color change, then there may instead have been a change in the "mantling" process, in which chromophores serving essentially as cloud condensation nuclei can become mantled by white ammonia ice, hiding their redness (West et al., 1986). Oval BA's cloud particles could have become denuded of their ammonia ice coatings, revealing red chromophores and resulting in an overall color change. The mantling process is favored by de Pater et al. (2010b) to explain the confinement of chromophores within Oval BA's red ring.

West et al. (1986) did not consider the condensation of reddish smog onto white icy nuclei, the inverse process to chromophore mantling. This process is similar to the coating hypothesis proposed to explain the scarcity of ammonia ice signatures in Jupiter's infrared spectrum (Atreya et al., 2005). Photochemistry of sulfur and phosphorous compounds is probably not rapid enough to produce red coatings, since the parent gases have low upper tropospheric mixing ratios. Kalogerakis et al. (2008) found that significant alteration of aerosol optical properties required coatings of thicknesses close to the radius of the original core particle. Chromophore mantling/unmantling via red coatings is therefore much more likely to work with red nuclei and white ammonia ice mantles, since ammonia is readily available and the condensation timescale is very fast compared to photochemical production timescales.

## 6.2. The color change

The red coloration in Oval BA has a radial distribution similar to the radial distribution of temperature, and the secondary circulation pattern near the top of the oval is directed radially outward. These factors suggest that the color change of Oval BA is somehow linked to temperature or circulation. Because Oval BA's circulation was unchanged, temperature is an appealing possibility as the underlying cause of the color change. A general temperature change is consistent with the prediction by Marcus (2004) that the merger of the White Ovals would alter equator-to-pole heat transport, producing an increase in low-latitude temperatures.

Studies have measured Jupiter's long-term upper tropospheric temperature variation (Orton et al., 1994; Simon-Miller et al., 2006a). However, these studies are focused on spatial variation of temperature, emphasizing relative meridional gradients rather than absolute values. These ground-based temperature studies are therefore valuable for studying relative changes in low-latitude temperature distributions, but a change in the absolute equator-to-

pole temperature contrast would not be detected without a reanalysis of all the data; the equator-to-pole temperature contrast has not actually been measured since the mergers of the White Ovals.

The unchanged circulation of Oval BA means that the temperature contrast ( $\Delta T$ ) between the oval and its surroundings stayed the same. But if temperatures changed by a small amount in the oval's surroundings, then temperatures would change likewise within the oval. A change in photochemical production of chromophores is consistent with an overall temperature increase, but not a temperature decrease, based on the radial increase in temperature within the oval. If decreasing temperatures led to the reddening of Oval BA, then the coldest part of the oval (the core) should be the reddest part of the oval.

de Pater et al. (2010b) commented that photochemically produced chromophores would rapidly fill the vortex within a few mixing times and produce isotropic redness, rather than a red annulus. But if dilution within the vortex is considered, then it should take many years for the vortex to become isotropically red, despite a short mixing timescale of several months. At least half the vortex volume needs to fill with chromophores before the upwelling material is red enough to eliminate Oval BA's red annulus, according to a simple mass mixing model. Assume that the photochemical production zone extends from the cloud base to the tropopause, and the full extent of the vortex reaches down to 5 bar. Then about 10% of the total mass of the vortex is within the photochemical production zone. If chromophores in this zone have a concentration of  $C$ , then after mixing through the vortex, the concentration in the upward return flow will be diluted to about 10%  $C$ . The upwelled chromophores could reach a higher concentration of about 50%  $C$  after some four or five mixing cycles within a closed system. But within that time, the oval's chromophore concentration would also be diluted by exchange between the oval and its environment due to turbulence, mergers with smaller anticyclones, and interaction with the ambient jet streams. Photochemical production of red chromophores is thus consistent with the observed long-lived radial color gradient, unless exchange with the environment is ignored, or unless mixing times are much faster than in de Pater et al. (2010b).

If coloration is controlled by ice mantles on red chromophore particles, the structure of Oval BA's red ring is easily explained, but the underlying cause of the color change is more difficult to discern. An overall temperature increase would reduce the ammonia ice column density, because ammonia condensation takes place at higher elevations and lower pressures in a warmer atmosphere. A comparison of two model cases with a 5 K temperature difference at the 400 mbar level—using the equilibrium cloud condensation model of Atreya and Romani (1985) and Atreya et al. (2003)—shows that the total ammonia ice cloud column density is lower by only about 9% for the warmer case, a relatively small change.

Column density is only part of the story, because most of this cloud mass will remain near the condensation level. The chromophores, on the other hand, seem to be located in the higher altitude haze layer, based on horizontal distributions in Fig. 7 and on prior work (e.g., Simon-Miller et al., 2001). So although the ammonia cloud has a slightly smaller column density in a warmer atmosphere, the flux of mantled chromophores up through the cloud base should be the same in both cases, because the secondary circulation (unchanged before and after the color change) basically acts as a dynamical filter, passing the smallest particles up into the haze. Throughout the column, the ammonia ice mantles may have some 10% less volume due to higher temperatures, but the population of small particles lofted up to the haze layer is probably not sensitive to this difference. An unchanged particle size distribution agrees with the observations of constant haze reflectivity before and after the color change, and the radiative transfer analysis of Pérez-Hoyos et al. (2009).

If an identical population of mantled chromophores drift radi- ally outward near the top of the vortex, but the environment is slightly warmer, then faster sublimation rates would result. This idea could be significantly bolstered by modeling studies including dynamics and microphysics.

Dredging of new red material from the depths of Jupiter's atmo- sphere, or new white material that transforms into red material, has also been invoked to explain the oval's color change (Simon- Miller et al., 2006b). Dredging of red material is much less likely than dredging of non-red precursor material, because there is no mechanism to keep red material confined to an annulus (de Pater et al., 2010b). Dredging involves changes in the vertical dimensions of the oval (deeper dredging) or in the mixing timescale (faster dredging). The vertical extent was constant, so deeper dredging is excluded. Faster dredging would require a shorter mixing time- scale. A significant change in the overall velocity field was not ob- served, implying (according to the scaling analysis in de Pater et al., 2010b) that the mixing time also has not changed.

## 7. Conclusions

We can identify no observed changes in Oval BA, other than col- or. We conclude that the vertical extent of the oval did not change, based mainly on the oval's velocity fields and its upper tropo- spheric haze reflectivity. The nearly constant haze reflectivity over time of Oval BA (and its progenitors) is a sign that the dynamical top of the oval did not change significantly. The high pressure anomaly at the core of the anticyclone did not change, based on velocity fields and the geostrophic approximation, so the anticy- clone did not turn red due to intensification. Modeling of velocity fields (Legarreta and Sánchez-Lavega, 2008; Shetty and Marcus, 2010) and cloud morphology (Cho et al., 2001) show that the static stability of Oval BA's environment was unchanged. Static stability is variable with altitude both in simulations and in the single deep measurement made by the Galileo Probe, so any change in the oval's height would make the oval sensitive to different values of static stability in the environment.

The magnitude of static stability required by vortex models ( $N \sim 0.08 \text{ s}^{-1}$  at 5–7 bar) is characteristic of the stratification pro- duced by condensation of water in supersolar abundance. The base of large vortices such as Oval BA and the GRS cannot be located at higher altitudes, because it would then be located in layers with weaker static stability, and vortex dynamics would differ from the observations. The vortex modeling work therefore supple- ments indirect evidence for supersolar water from the depth of lightning, the disequilibrium abundance of tropospheric CO, the depths of observed clouds, and 5- $\mu\text{m}$  spectroscopy (as reviewed in Wong et al., 2008).

A change in temperatures within the oval and its surroundings is an intriguing but controversial explanation for the color change. Velocity field results mean that the thermodynamic anomalies of the oval did not change significantly (de Pater et al., 2010b; Marcus et al., 2011), so the difference in temperature between the oval and its surroundings is the same, and a temperature change within the oval can only result from a change in the temperature of the sur- roundings. New models encompassing the uncertainties in the velocity retrievals could better quantify how much the structure of Oval BA may have really changed given the qualitatively identi- cal velocity fields in 2000, 2006, and 2009.

The color change most likely led to reddening of the oval via one of two chromophore processes: a change in the photochemical production rate of red material, or a change in the mantling process in which white  $\text{NH}_3$  ice condenses onto and hides red chromophore nuclei. Either process is consistent with a temperature increase, but the limited knowledge of these chromophore processes makes

it difficult to quantify even such basic parameters as the amount of temperature change needed to create a color change. Voyager IRIS and Cassini CIRS measured temperatures on Jupiter using the infra- red S(0) and S(1) hydrogen absorption lines, but no similar temper- ature measurement has been conducted after 2000 because these lines fall at wavelengths of low terrestrial atmospheric transmit- tance. The MIRI instrument on the James Webb Space Telescope will be able to observe Jupiter at these wavelengths (Lunine et al., 2010).

## Acknowledgments

The jovian cloud imaging data presented in this paper were ob- tained with the NASA/ESA Hubble Space Telescope. These observa- tions are associated with HST GO Programs 10782, 11102, and 11559, with support provided by NASA through a grant from the Space Telescope Science Institute (STScI), which is operated by the Association of Universities for Research in Astronomy, Inc., un- der NASA contract NAS 5-26555. Additional archival WFPC2 and ACS observations were obtained from the Data Archive at STScI, associated with the programs listed in Table 1. Analysis was sup- ported by the Astronomy and Astrophysics Program of NSF and by the Berkeley-France fund. We thank Sean Lockwood and Patrick Lii for developing HST data reduction code, Ashwin Vasavada for sharing processed Cassini imaging data, William Januszewski (STScI) for his patience and effort in accommodating the strict tim- ing constraints of our Jupiter observations, Mona Delitsky for help- ful discussions about chromophore chemistry, and Erich Karkoschka for insight into the characteristics of WFPC2's meth- ane-band filter. The helpful and collegial comments from two anonymous reviewers led to major improvements in this paper.

## References

- Achterberg, R.K., Conrath, B.J., Gierasch, P.J., 2006. Cassini CIRS retrievals of ammonia in Jupiter's upper troposphere. *Icarus* 182, 169–180.
- Asay-Davis, X., Marcus, P.S., Wong, M.H., de Pater, I., 2009. Jupiter's shrinking Great Red Spot and steady Oval BA: Velocity measurements with the 'Advection Corrected Correlation Image Velocimetry' automated cloud-tracking method. *Icarus* 203, 164–188.
- Atreya, S.K., Romani, P.N., 1985. Photochemistry and clouds of Jupiter, Saturn and Uranus. In: Hunt, G.E. (Ed.), *Recent Advances in Planetary Meteorology*. Cambridge University Press, New York, pp. 17–68.
- Atreya, S.K., Wong, M.H., Owen, T.C., Niemann, H.B., Mahaffy, P.R., 1997. Chemistry and clouds of the atmosphere of Jupiter: A Galileo perspective. In: Barbieri, C., Rahe, J.H., Johnson, T.V., Sohus, A.M. (Eds.), *Three Galileos: The Man, The Spacecraft, The Telescope*. Kluwer Academic, Dordrecht, The Netherlands, pp. 249–260.
- Atreya, S.K., Mahaffy, P.R., Niemann, H.B., Wong, M.H., Owen, T.C., 2003. Composition of the atmosphere of Jupiter—An update, and implications for the extrasolar giant planets. *Planet. Space Sci.* 51, 105–112.
- Atreya, S.K., Wong, A.S., Baines, K.H., Wong, M.H., Owen, T.C., 2005. Jupiter's ammonia clouds—localized or ubiquitous? *Planet. Space Sci.* 53, 498–507.
- Aubert, O., 2010. Form and persistence of a vortex in a rotating and stratified fluid. Thesis, Technopôle de Château-Gombert, Marseille, France.
- Aubert, O., Le Bars, M., Le Gal, P., Marcus, P.S., 2010. Universal scaling law for the aspect ratio of a pancake vortex in a rotating stratified medium. American Physical Society Division of Fluid Dynamics Meeting, 22 November, 2010. <<http://www.meetings.aps.org/link/BAPS.2010.DFD.LH.10>>.
- Baines, K.H., Delitsky, M.L., Momary, T.W., Carlson, R.W., Orton, G.S., 2004. Seeing red: Chromophores, clouds, and chemistry in Jupiter's Great Red Spot. *Bull. Am. Astron. Soc.* 36, 1133.
- Banfield, D., Conrath, B.J., Gierasch, P.J., Nicholson, P.D., Matthews, K., 1998a. Near-IR spectrophotometry of jovian aerosols – Meridional and vertical distributions. *Icarus* 134, 11–23.
- Banfield, D., Gierasch, P.J., Bell, M., Ustinov, E., Ingersoll, A.P., Vasavada, A.R., West, R.A., Belton, M.J.S., 1998b. Jupiter's cloud structure from Galileo imaging data. *Icarus* 135, 230–250.
- Beebe, R.F., Hockey, T.A., 1986. A comparison of red spots in the atmosphere of Jupiter. *Icarus* 67, 96–105.
- Cheng, A.F., Simon-Miller, A.A., Weaver, H.A., Baines, K.H., Orton, G.S., Yanamandra-Fisher, P.A., et al., 2008. Changing characteristics of Jupiter's Little Red Spot. *Astron. J.* 135, 2446–2452.
- Cho, J.Y.-K., de la Torre Juárez, M., Ingersoll, A.P., Dritschel, D.G., 2001. A high-resolution, three-dimensional model of Jupiter's Great Red Spot. *J. Geophys. Res.* 106, 5099–5106.

- Choi, D.S., Showman, A.P., Vasavada, A.R., 2010. The evolving flow of Jupiter's White Ovals and adjacent cyclones. *Icarus* 207, 359–372.
- Conrath, B.J., Gierasch, P.J., 1984. Global variation of the para hydrogen fraction in Jupiter's atmosphere and implications for dynamics on the outer planets. *Icarus* 57, 184–204.
- Conrath, B.J., Gierasch, P.J., Leroy, S.S., 1990. Temperature and circulation in the stratosphere of the outer planets. *Icarus* 83, 255–281.
- Conrath, B.J., Gierasch, P.J., Nath, N., 1981. Stability of zonal flows on Jupiter. *Icarus* 48, 256–282.
- de Pater, I., Wong, M.H., de Kleer, K., Hammel, H.B., Ádámkóvics, M., Conrad, A., 2011. Keck adaptive optics images of Jupiter's north polar cap and Northern Red Oval. *Icarus* 213, 559–563.
- de Pater, I., Fletcher, L.N., Pérez-Hoyos, S., Hammel, H.B., Orton, G.S., Wong, M.H., Luszcz-Cook, S., Sánchez-Lavega, S., Boslough, M., 2010a. A multi-wavelength study of the 2009 impact on Jupiter: Comparison of high resolution images from Gemini, Keck and HST. *Icarus* 210, 722–741.
- de Pater, I., Wong, M.H., Marcus, P.S., Luszcz-Cook, S., Ádámkóvics, M., Conrad, A., Asay-Davis, X., Go, C., 2010b. Persistent rings in and around Jupiter's anticyclones – Observations and theory. *Icarus* 210, 742–762.
- Delitsky, M.L., Baines, K.H., 2007. Jupiter's Great Red Spot: Cloud chemistry and chromophore formation. *Bull. Am. Astron. Soc.* 38, 444.
- Edgington, S.G., Atreya, S.K., Trafton, L.M., Caldwell, J.J., Beebe, R.F., Simon, A.A., West, R.A., 1999. Ammonia and eddy mixing variations in the upper troposphere of Jupiter from HST faint object spectrograph observations. *Icarus* 142, 342–356.
- Fincham, A., Delerce, G., 2000. Advanced optimization of correlation imaging velocimetry algorithms. *Exp. Fluids* 29, 13–22.
- Fincham, A.M., Spedding, G.R., 1997. Low cost, high resolution DPIV for measurement of turbulent fluid flow. *Exp. Fluids* 23, 449–462.
- Flasar, F.M., Conrath, B.J., Pirraglia, J., Clark, P.C., French, R.G., Gierasch, P.J., 1981. Thermal structure and dynamics of the Jovian atmosphere. I – The Great Red SPOT. *J. Geophys. Res.* 86, 8759–8767.
- Flasar, F.M., 1989. Temporal behavior of Jupiter's meteorology. In: Belton, M.J.S., West, R.A., Rahe, J. (Eds.), *Time-Variability Phenomena in the Jovian System*. NASA SP-494, Washington, DC, pp. 324–343.
- Fletcher, L.N., Orton, G.S., Mousis, O., Yanamandra-Fisher, P., Parrish, P.D., Irwin, P.G.J., Fisher, B.M., Vanzi, L., Fujiyoshi, T., Fuse, T., Simon-Miller, A.A., Edkins, E., Hayward, T.L., De Buizer, J., 2010. Thermal structure and composition of Jupiter's Great Red Spot from high-resolution thermal imaging. *Icarus* 208, 306–328.
- Friedson, A.J., 2005. Water, ammonia and H<sub>2</sub>S mixing ratios in Jupiter's 5-micron hot spots: A dynamical model. *Icarus* 177, 1–17.
- Fruchter, A., Sosey, M. (Eds.), 2009. *The MultiDrizzle Handbook*, Version 3.0. Space Telescope Science Institute, Baltimore, MD.
- Gierasch, P.J., Goody, R.M., 1969. Radiative time constant in the atmosphere of Jupiter. *J. Atmos. Sci.* 26, 979–980.
- Go, C.Y., de Pater, I., Wong, M.H., Lockwood, S., Marcus, P., Asay-Davis, X., et al., 2006. Evolution of the Oval BA during 2004–2005. *Bull. Am. Astron. Soc.* 38, 495.
- Gonzaga, S., Biretta, J. (Eds.), 2010. *HST WFPC2 Data Handbook*, Version 5.0. Space Telescope Science Institute, Baltimore, MD.
- Grevesse, N., Asplund, M., Sauval, A.J., 2007. The solar chemical composition. *Space Sci. Rev.* 130, 105–114.
- Griffith, C.A., Bevard, B., Owen, T., Gautier, D., 1992. The tropospheric abundances of NH<sub>3</sub> and PH<sub>3</sub> in Jupiter's Great Red Spot, from Voyager IRIS observations. *Icarus* 98, 82–93.
- Hueso, R., Legarreta, J., García-Melendo, E., Sánchez-Lavega, A., Pérez-Hoyos, S., 2009. The jovian anticyclone BA. II. Circulation and interaction with the zonal jets. *Icarus* 203, 499–515.
- Kalirai, J.S., MacKenty, J., Rajan, A., Baggett, S., Bohlin, R., Brown, T., et al., 2009. WFC3 SMOV Proposal 11450: The Photometric Performance and Calibration of WFC3/UVIS. Instrument Science Report WFC3 2009-31. Space Telescope Science Institute, Baltimore, MD.
- Kalogerakis, K.S., Marschall, J., Oza, A.U., Engel, P.A., Meharchand, R.T., Wong, M.H., 2008. The coating hypothesis for ammonia ice particles in Jupiter: Laboratory experiments and optical modeling. *Icarus* 196, 202–215.
- Karkoschka, E., 1994. Spectrophotometry of the jovian planets and Titan at 300– to 1000-nm wavelength: The methane spectrum. *Icarus* 111, 174–192.
- Karkoschka, E., Koekemoer, A.M., 2002. WFPC2 flatfields with reduced noise and an anomaly of filter FQCH4N-D. In: Arribas, S., Koekemoer, A., Whitmore, B. (Eds.), *The 2002 HST Calibration Workshop: Hubble after the Installation of the ACS and the NICMOS Cooling System*. Space Telescope Science Institute, Baltimore, MD, pp. 315–324.
- Krasnopolsky, V.A., 2007. Chemical kinetic model for the lower atmosphere of Venus. *Icarus* 191, 25–37.
- Kundu, P.K., 1990. *Fluid Mechanics*. Academic Press, San Diego, CA.
- Lebofsky, L.A., Fegley, M.B., 1976. Laboratory reflection spectra for the determination of chemical composition of icy bodies. *Icarus* 28, 379–387.
- Legarreta, J., Sánchez-Lavega, A., 2008. Vertical structure of Jupiter's troposphere from nonlinear simulations of long-lived vortices. *Icarus* 196, 184–201.
- Li, L., Ingersoll, A.P., Vasavada, A.R., Simon-Miller, A.A., Del Genio, A.D., Ewald, S.P., et al., 2006. Vertical wind shear on Jupiter from Cassini images. *J. Geophys. Res. (Planets)* 111, E04004.
- Lii, P.S., Wong, M.H., de Pater, I., 2010. Temporal variation of the tropospheric cloud and haze in the jovian equatorial zone. *Icarus* 209, 591–601.
- Lindal, G.F., Wood, G.E., Levy, G.S., Anderson, J.D., Sweetnam, D.N., Hotz, H.B., et al., 1981. The atmosphere of Jupiter – An analysis of the Voyager radio occultation measurements. *J. Geophys. Res.* 86, 8721–8727.
- Lunine, J., Hammel, H., Shaller, E., Sonneborn, G., Orton, G., Rieke, G., et al., 2010. JWST Planetary Observations within the Solar System. White paper. <[http://www.stsci.edu/jwst/doc-archive/white-papers/JWST\\_Solar\\_System.pdf](http://www.stsci.edu/jwst/doc-archive/white-papers/JWST_Solar_System.pdf)>.
- Magalhães, J.A., Seiff, A., Young, R.E., 2002. The stratification of Jupiter's troposphere at the Galileo Probe entry site. *Icarus* 158, 410–433.
- Marcus, P.S., 2004. Prediction of a global climate change on Jupiter. *Nature* 428, 828–831.
- Marcus, P.S., Asay-Davis, X., Wong, M.H., de Pater, I., 2011. Jupiter's new red oval: Dynamics, color, and relationship to jovian climate change. *J. Heat Transfer*, in press.
- Massie, S.T., Hunten, D.M., 1982. Conversion of para and ortho hydrogen in the jovian planets. *Icarus* 49, 213–226.
- Matcheva, K.I., Conrath, B.J., Gierasch, P.J., Flasar, F.M., 2005. The cloud structure of the jovian atmosphere as seen by the Cassini/CIRS experiment. *Icarus* 179, 432–448.
- Maybhatte, A. (Ed.), 2010. *ACS Instrument Handbook*, Version 9.0. Space Telescope Science Institute, Baltimore, MD.
- McMaster, M., Biretta, J. (Eds.), 2008. *WFPC2 Instrument Handbook*, Version 10.0. Space Telescope Science Institute, Baltimore, MD.
- Nakajima, K., Takehiro, S.-I., Ishiwatari, M., Hayashi, Y.-Y., 2000. Numerical modeling of Jupiter's moist convection layer. *Geophys. Res. Lett.* 27, 3129–3132.
- Niemann, H.B., Atreya, S.K., Carignan, G.R., Donahue, T.M., Haberman, J.A., Harpold, D.N., et al., 1998. The composition of the jovian atmosphere as determined by the Galileo Probe Mass Spectrometer. *J. Geophys. Res.* 103, 22831–22846.
- Orton, G.S., Fisher, B.M., Baines, K.H., Stewart, S.T., Friedson, A.J., Ortiz, J.L., et al., 1998. Characteristics of the Galileo probe entry site from Earth-based remote sensing observations. *J. Geophys. Res.* 103, 22791–22814.
- Orton, G.S., Friedson, A.J., Yanamandra-Fisher, P.A., Caldwell, J., Hammel, H.B., Baines, K.H., et al., 1994. Spatial organization and time dependence of Jupiter's tropospheric temperatures, 1980–1993. *Science* 265, 625–631.
- Pedlosky, J., 1987. *Geophysical Fluid Dynamics*. Springer-Verlag, New York, NY.
- Peek, B.M., 1958. *The Planet Jupiter*. Faber and Faber, London.
- Pérez-Hoyos, S., Sánchez-Lavega, A., Hueso, R., García Melendo, E., Legarreta, J., 2009. The jovian anticyclone BA. III. Aerosol properties and color change. *Icarus* 203, 516–530.
- Porco, C.C., West, R.A., McEwen, A., Del Genio, A.D., Ingersoll, A.P., Thomas, P., et al., 2003. Cassini imaging of Jupiter's atmosphere, satellites, and rings. *Science* 299, 1541–1547.
- Sánchez-Lavega, A., Rojas, J.F., Hueso, R., Lecacheux, J., Colas, F., Acarreta, J.R., Miyazaki, I., Parker, D., 1999. Interaction of jovian white Ovals BC and DE in 1998 from Earth-based observations in the visual range. *Icarus* 142, 116–124.
- Sánchez-Lavega, A., Orton, G.S., Morales, R., Lecacheux, J., Colas, F., Fisher, B., Fukumura-Sawada, P., Golisch, W., Griep, D., Kaminski, C., Baines, K., Rages, K., West, R., 2001. NOTE: The Merger of Two Giant Anticyclones in the Atmosphere of Jupiter. *Icarus* 149, 491–495.
- Sayanagi, K.M., Mitchell, J., Ingersoll, A.P., Ewald, S.P., Marcus, P.S., de Pater, I., et al., 2010. A benchmark for cloud tracking wind measurements. *AGU (Fall Suppl.) Abstracts A1335*.
- Seiff, A., Kirk, D.B., Knight, T.C.D., Young, R.E., Mihalov, J.D., Young, L.A., et al., 1998. Thermal structure of Jupiter's atmosphere near the edge of a 5- $\mu$ m hot spot in the north equatorial belt. *J. Geophys. Res.* 103, 22857–22890.
- Shetty, S., Marcus, P.S., 2010. Changes in Jupiter's Great Red Spot (1979–2006) and Oval BA (2000–2006). *Icarus* 210, 182–201.
- Shetty, S., Asay-Davis, X.S., Marcus, P.S., 2007. On the interaction of Jupiter's Great Red Spot and zonal jet streams. *J. Atmos. Sci.* 64, 4432–4444.
- Showman, A.P., Dowling, T.E., 2000. Nonlinear simulations of Jupiter's 5-micron hot spots. *Science* 289, 1737–1740.
- Showman, A.P., Ingersoll, A.P., 1998. Interpretation of Galileo probe data and implications for Jupiter's dry downdrafts. *Icarus* 132, 205–220.
- Sill, G.T., 1973. Reflection spectra of solids of planetary interest. *Commun. Lunar Planet. Lab. No.* 184, 10, 1–7.
- Simon-Miller, A.A., Conrath, B.J., Gierasch, P.J., Orton, G.S., Achterberg, R.K., Flasar, F.M., Fisher, B.M., 2006a. Jupiter's atmospheric temperatures: From Voyager IRIS to Cassini CIRS. *Icarus* 180, 98–112.
- Simon-Miller, A.A., Chanover, N.J., Orton, G.S., Sussman, M., Tsaviris, I.G., Karkoschka, E., 2006b. Jupiter's White Oval turns red. *Icarus* 185, 558–562.
- Simon-Miller, A.A., Banfield, D., Gierasch, P.J., 2001. Color and the vertical structure in Jupiter's belts, zones, and weather systems. *Icarus* 154, 459–474.
- Sromovsky, L.A., Fry, P.M., 2010. The source of widespread 3- $\mu$ m absorption in Jupiter's clouds: Constraints from 2000 Cassini VIMS observations. *Icarus* 210, 230–257.
- Sromovsky, L.A., Fry, P.M., 2002. Jupiter's cloud structure as constrained by Galileo Probe and HST observations. *Icarus* 157, 373–400.
- Strycker, P.D., Chanover, N., Sussman, M., Simon-Miller, A., 2006. A spectroscopic search for Jupiter's chromophores. *Bull. Am. Astron. Soc.* 38, 498.
- Sugiyama, K., Odaka, M., Nakajima, K., Hayashi, Y.-Y., 2009. Development of a cloud convection model to investigate the Jupiter's atmosphere. *Nagare Multimedia*. <<http://www2.nagare.or.jp/mmm/2009/sugiyama/>>.
- Sugiyama, K., Odaka, M., Kuramoto, K., Hayashi, Y.-Y., 2006. Static stability of the jovian atmospheres estimated from moist adiabatic profiles. *Geophys. Res. Lett.* 33, L03201.
- Tody, D., 1993. IRAF in the Nineties. In: Hanisch, R.J., Brissenden, R.J.V., Barnes, J. (Eds.), *Astronomical Data Analysis Software and Systems II*. A.S.P. Conference Series, vol. 52, pp. 173–183.
- Tokunaga, A.T., Ridgway, S.T., Knacke, R.F., 1980. High spatial and spectral resolution 10-micron observations of Jupiter. *Icarus* 44, 93–101.

- van Dokkum, P.G., 2001. Cosmic-ray rejection by Laplacian edge detection. *Publ. Astron. Soc. Pacific* 113, 1420–1427.
- Vasavada, A.R., Hörst, S.M., Kennedy, M.R., Ingersoll, A.P., Porco, C.C., Del Genio, A.D., et al., 2006. Cassini imaging of Saturn: Southern hemisphere winds and vortices. *J. Geophys. Res. (Planets)* 111, E05004.
- West, R.A., Baines, K.H., Friedson, A.J., Banfield, D., Ragent, B., Taylor, F.W., 2004. Jovian clouds and haze. In: Bagenal, F., Dowling, T.E., McKinnon, W.B. (Eds.), *Jupiter*. Cambridge University Press, Cambridge, pp. 79–104.
- West, R.A., Strobel, D.F., Tomasko, M.G., 1986. Clouds, aerosols, and photochemistry in the jovian atmosphere. *Icarus* 65, 161–217.
- Wong, M.H., 2010. Amplitude of fringing in WFC3/UVIS narrowband red filters. Instrument Science Report WFC3 2010-04. Space Telescope Science Institute, Baltimore, MD.
- Wong, M.H., 2009. Comment on “Transport of nonmethane hydrocarbons to Jupiter’s troposphere by descent of smog particles” by Donald M. Hunten, 2008 [*Icarus* 194, 616–622]. *Icarus* 199, 231–235.
- Wong, M.H., Pavlovsky, C., Long, K.S. (Eds.), 2010. *Wide Field Camera 3 Instrument Handbook, Version 2.0*. Space Telescope Science Institute, Baltimore, MD.
- Wong, M.H., Lunine, J., Atreya, S.K., Johnson, T., Mahaffy, P.R., Owen, T.C., et al., 2008. Oxygen and other volatiles in the giant planets and their satellites. In: MacPherson, G.J., Mittlefehldt, D.W., Jones, J., Simon, S.B. (Eds.), *Oxygen in the Solar System, Reviews in Mineralogy and Geochemistry*, vol. 68. Mineralogical Society of America, Chantilly, VA, pp. 219–246.
- Wong, M.H., Mahaffy, P.R., Atreya, S.K., Niemann, H.B., Owen, T.C., 2004. Updated Galileo Probe Mass Spectrometer measurements of carbon, oxygen, nitrogen, and sulfur on Jupiter. *Icarus* 171, 153–170.
- Young, R.E., 2003. The Galileo probe: How it has changed our understanding of Jupiter. *New Astron. Rev.* 47, 1–51.
- Youssef, A., Marcus, P.S., 2003. The dynamics of jovian white ovals from formation to merger. *Icarus* 162, 74–93.
- Zuchowski, L.C., Yamazaki, Y.H., Read, P.L., 2009. Modeling Jupiter’s cloud bands and decks. 1. Jet scale meridional circulations. *Icarus* 200, 548–562.